

Reduced-order computational homogenization for hyperelastic media using gradient based sensitivity analysis of microstructures

Vladimír Lukeš^a, Eduard Rohan^a

^a*Department of Mechanics & NTIS – New Technologies for Information Society Research Centre, Faculty of Applied Sciences, University of West Bohemia in Pilsen, Univerzitní 8, Plzeň, 30100, Czech Republic*

Abstract

We propose an algorithm for the computational homogenization of locally periodic hyperelastic structures undergoing large deformations due to external quasi-static loading. The algorithm performs clustering of macroscopic deformations into subsets called “centroids”, and, as a new ingredient, approximates the homogenized coefficients using sensitivity analysis of micro-configurations with respect to the macroscopic deformation. The novel “model-order reduction” approach significantly reduces the number of microscopic problems that must be solved in nonlinear simulations, thereby accelerating the overall computational process. The degree of reduction can be controlled by a user-defined error tolerance parameter. The algorithm is implemented in the finite element framework *SfePy*, and its performance effectiveness is demonstrated using two-dimensional test examples, when compared with solutions obtained by the proper orthogonal decomposition method, and by the full “FE-square” simulations. Extensions beyond the present implementations and the scope of tractable problems are discussed.

Keywords: Multiscale modelling, Model order reduction, Large deformation, Asymptotic homogenization, Sensitivity analysis, K-means clustering

1. Introduction

The *computational homogenization (CH)*, as an alternative to the phenomenological macroscopic modelling, see e.g. [1, 2], belongs to the most relevant modelling methods for analyses of nonlinear problems in continuum mechanics when the model can be characterized at multiple scales, whereby at least a “microscopic” scale can be described in terms of continuum models defined in locally periodic structures using geometrical features which are related to microstructure heterogeneities. In general, the CH replaces the solution of a problem defined at the scale of distinguished locally periodic heterogeneities by solutions obtained for a smeared continuum occupied by an equivalent homogeneous material. This is characterized by effective material coefficients which are obtained by solving appropriate boundary value problems in the *representative volume elements (RVE)*, often called the “reference periodic unit cell” in the homogenization community. Besides the CH based on “numerical testing” the RVE of the microstructure, by applying the “macroscopic strain modes”, also the “asymptotic analysis based homogenization”, cf. [3, 4], leads to analogous CH algorithms, featured by the similar hurdles arising due to the two-scale coupling between the global “macroscopic” and the local “microscopic” nonlinear responses.

For linear problems, especially when perfectly periodic media are considered, the homogenization significantly reduces the computational cost of solving the global macroscopic problem for a given finite heterogeneity size, i.e. when the scale parameter $\varepsilon = \varepsilon_0 > 0$ (the one involved in the asymptotic analysis of homogenization) is nonvanishing, with given the microscopic and the macroscopic characteristic lengths, denoted by ℓ and L , respectively, such that $\varepsilon_0 = \ell/L$. By virtue of the asymptotic homogenization result, the effective medium properties, like the elasticity tensor involved in the macroscopic problem, are expressed by the characteristic responses of the *representative periodic cell (RPC)* are solved independently of the macroscopic problem. To get refined response at the heterogeneity scale, the macroscopic solution (such as macroscopic strains) can be combined “point-wise” with the characteristic responses, to obtain the micro-scale field (the

Email addresses: vlukes@kme.zcu.cz (Vladimír Lukeš), rohan@kme.zcu.cz (Eduard Rohan)

displacements) at the local RVE, defined as a copy of the RPC. In this way, the macroscopic domain can be covered by a “tiling” so that the refined solution is obtained in the whole structure, cf. [5] where this issue was discussed in the large deformation setting. This so-called reconstruction step of the two-scale modelling is optional and can also be done only selectively at locations of interest within the macroscopic domain, see e.g. [6] for an application in porous media modelling. In the context of small deformations and linear material models, computational homogenization is a well-established and widely used method for modeling, e.g. elastic structures [7], viscoelastic and porous media [8, 9, 10, 6], as well as thermo-mechanical processes [11]. The idea of locally refined response has been developed in [12] on the basis of the so-called Homogenized Dirichlet Projection Method. Recently, an efficient method for the global-local analysis related to linear higher-order gradient media was proposed in [13].

In nonlinear problems, see e.g. [14], the effective material parameters depend locally on the macroscopic state, and the full-scale decoupling that is applicable to linear models cannot be employed. The finite element method is applied for the spatial discretization at both the macroscopic and the microscopic scales, such that the so approximated macroscopic problem formulation and the “microscopic” problems imposed in the local RVEs, are coupled due to the nonlinear behavior. In this context, within the framework of the so-called *FE-square* (FE^2) computational strategy [15, 16, 17], a microscopic problem is usually solved at each quadrature point of the macroscopic domain, providing homogenized parameters that are valid locally only at that macroscopic point. Although the FE^2 strategy can provide accurate solutions of the two-scale problem, it becomes extremely computationally demanding, as it requires repeated solutions of the coupled micro-macro problems within many steps of the iterative algorithm. An extreme computational effort is observed mainly in three-dimensional problems with complex macroscopic geometries, where achieving sufficient accuracy of the macroscopic solution requires a large number of finite elements in the spatial discretization or higher-order approximations, both of which increase the number of microscopic problems that must be solved.

To bypass this computational cost, numerous approximation strategies have been proposed (e.g. [18, 17, 19] for hyperelastic structures and [20, 21] for elasto-plastic materials), most of which are based on the *proper orthogonal decomposition* (*POD*) which enables an efficient reduction of the discretized microscopic subproblems dimension using a precomputed reduced basis. However, as the number of degrees of freedom of the microscopic discretization grows, the computation of this basis also becomes increasingly expensive, because it requires solving an eigenvalue problem for large dense systems. As an alternative to *POD*-based approaches, methods relying on the approximation of the homogenized parameters using trained artificial neural networks have also been developed [22], employing convolutional [23, 24] or recurrent [25] network architectures. Furthermore, in [26, 27], the reduction of computational complexity in nonlinear models is achieved through the clustering of subdomains at the level of periodic unit cells.

Although the above mentioned *model order reduction* (*MOR*) approaches to the multiscale numerical modeling for nonlinear problems seem to provide significant improvements relative to the direct and very costly FE^2 method of the computational homogenization, the following challenges can be seen:

Ch1: To minimize the off-line computations, as used in the *POD* approach: the precomputed solutions of the microscopic problem for various *macroscopic deformation states* (*MDS*) are typically obtained for a range of macroscopic deformations containing a lot of *MDS* which are not used, i.e. do not appear in the specific macroscopic problem.

Ch2: To enable an efficient solving of a two-scale design optimization problem leading to functionally graded materials: the microstructure response depends on the *MDS* and also on the local design, i.e. the microscopic configuration requires another extra parameterization by the design variables. In this context, the *POD* off-line stage would be even more demanding.

Ch3: The clustering approach used, e.g. in [28, 29], needs to establish an approximation scheme within each cluster of similar *MDS*; for this, typically AI-based (machine learning) methods are employed to solve the micro-problems. A common problem with this clustering approach arises from the inconsistency between the continuous evolution of the deformation, whereas the macroscopic properties (typically the tangent elasticity and the stress) are changing abruptly when the particular macroscopic point switches from one cluster to another between two consecutive iterations. Heuristic algorithms (like cluster freezing, cf. [29])

have been proposed in an effort to remedy this effect, which otherwise may stop the convergence of the macroscopic iterations. One may ask for alternative approaches to construct an approximation scheme over the set of all MDS represented by a limited number of clusters, each associated with a single microstructure and its microscopic deformation state.

Paper contribution. In response to these challenges, we propose a new MOR-based method called “Clustering and Sensitivity-based Approximation” (CSA) intended for the two-scale computational homogenization. This method has the following features, which also characterize the contributions of the present work:

- The macroscopic properties of the homogenized medium are recovered in the entire domain using an approximation scheme based on the clustering approach, providing a continuous transition of the MDS from one centroid to another. This feature remedies the convergence issues observed in related works, see above Challenge 3.
- Within each subdomain of the macroscopic body associated with a cluster, the homogenized properties are given by the representative microstructure of the cluster centroid associated with a MDS. To establish the homogenized properties at a macroscopic position belonging to the cluster, a linear mapping is constructed in the centroid using the sensitivity analysis of the macroscopic tangent elastic modulus and the effective stress w.r.t. the MDS variations. For this, the domain method of differentiation known from the shape optimization is adapted. The so-called “design velocity field” is presented by the microstructure displacement correctors (in the language of the asymptotic homogenization), the characteristic response of the microstructure w.r.t. the macroscopic deformation mode. The linear mapping is applied to relative MDS variations of stretches evaluated using the polar decomposition of the deformation gradient. Note that, in [29], the “linear approximation within the centroid” is given for effective stresses only using the tangent elastic modulus which, however, is constant within the cluster.
- The CSA method does not rely on any “off-line” stage of the numerical modeling (see Challenge 1 above): the representative microstructures are introduced “on-flight” as the macroscopic deformation progresses. This approach significantly reduces the number of microscopic problems that need to be solved compared to the POD-based approach.
- Although the proposed CSA method is developed and tested for hyperelastic materials, the approximation scheme can be generalized within the same framework to include: a) functionally graded materials, i.e. to account for quasi-periodic microstructures evolving with the position variation through the macroscopic body – the issue pertinent for two-scale design optimization, see above Challenge 2; b) dependence of the microscopic configuration on internal variables, such as inelastic deformation, cf. [28, 29]. It is worth noting that the extended parametrization by such additional variables (design, or internal variables) is much less expensive in the sense of computational complexity for the “on-flight” approach used in the CSA method than the analogous extension for the “off-line” approach of pre-computed microstructure responses, such as the POD method, requiring to get responses for the Cartesian product of intervals for the considered micro-configuration parameters. Therefore, the CSA method can be of particular interest for two-scale structural optimization based on homogenization.

To demonstrate the computational efficiency and illustrate some of the above claimed features, the proposed CSA method is compared with the full FE^2 simulation and the POD method. The algorithms of both the MOR methods are implemented within the SfePy framework [30] and the source code is available in the public repository [31].

Paper organization. The paper is organized as follows. Section 2 introduces the formulation of the large deformation analysis in heterogeneous hyperelastic structures. Section 3 outlines the two-scale homogenization framework, which yields the local subproblems described in Section 3.1 and the global problem with homogenized coefficients in Section 3.2. The approximation strategy for the homogenized coefficients is developed in Section 4. The complete CSA algorithm is presented in Section 5. Section 6 provides a brief overview of the POD method. Finally, Section 7 presents several numerical experiments designed to assess the approximation error and demonstrate the efficiency of the CSA in comparison with the FE^2 and POD methods.

Notation. Throughout this paper, the following notation is used. Since the problem involves two spatial scales, we distinguish between the macroscopic coordinates x and the microscopic coordinates y . By $\partial_i = \partial_i^x$ we abbreviate the partial derivative $\partial/\partial x_i$. We use $\nabla_x = (\partial_i^x)$ and $\nabla_y = (\partial_i^y)$ when differentiation w.r.t. coordinate x and y is used, respectively. By $\varepsilon = \ell/L$ we denote the scale parameter, relating the microscopic length ℓ to the macroscopic one L . Boldface symbols are used to represent vectors $\mathbf{a} = (a_i)$ and second-order tensors $\mathbf{b} = (b_{ij})$. The fourth-order elasticity tensor is denoted by $\mathbf{A} = (A_{ijkl})$ or $\mathbf{D} = (D_{ijkl})$. The homogenized coefficients are written as $\mathcal{A} = (\mathcal{A}_{ijkl})$ and $\mathcal{S} = (\mathcal{S}_{ij})$. The second-order identity tensor is represented by $\mathbf{I} = (\delta_{ij})$ and $\mathbf{e}(\mathbf{u}) = 1/2(\nabla\mathbf{u} + \nabla\mathbf{u}^T)$ is the linear strain tensor of a vector field \mathbf{u} . The dot symbol ‘ \cdot ’ denotes the scalar product of two vectors, while the colon ‘ $:$ ’ represents the inner product of two second-order tensors. The Sobolev spaces $H^1(Y)$ of the square-integrable functions up to the 1st order generalized derivative, defined in domain Y . For vector-valued functions the bold notation is applied \mathbf{H}^1 . Subspaces of Y -periodic functions are employed for vector-valued functions are denoted by $\mathbf{H}_{\#}^1(Y)$.

2. Hyperelastic structures – problem formulation

We consider a compressible hyperelastic material, occupying an open bounded domain $\Omega^\varepsilon \in \mathbb{R}$, whose mechanical behavior is governed by the neo-Hookean material model. The Cauchy stress tensor is expressed in terms of the bulk modulus K^ε and the shear modulus μ^ε as

$$\boldsymbol{\sigma}^\varepsilon = K^\varepsilon(J - 1)\mathbf{I} + \mu^\varepsilon J^{-5/3}(\mathbf{b} - \text{tr}(\mathbf{b})/3\mathbf{I}), \quad (1)$$

where \mathbf{F} is the deformation gradient, $J = \det(\mathbf{F})$ is the relative volume change, $\mathbf{b} = \mathbf{F}\mathbf{F}^T$ is the left Cauchy-Green deformation tensor, $\mathbf{I} = (\delta_{ij})$ is the Kronecker symbol, and $\text{tr}(\mathbf{b}) = b_{ii}$ is the trace of \mathbf{b} . The superscript ε indicates spatially fluctuating quantities depending on the scale parameter ε , otherwise employed in the asymptotic homogenization analysis. We demonstrate our computational method using the simple two-parametric neo-Hookean model. However, the derivations presented in the following sections are general enough to employ more complex material models such as Mooney-Rivlin, Ogden, or Yeoh. In the Eulerian frame, the constitutive equation (1), together with the equilibrium equation imposed in the deformed configuration,

$$-\nabla \cdot \boldsymbol{\sigma}^\varepsilon = \mathbf{f}^\varepsilon, \quad \text{in } \Omega^\varepsilon, \quad (2)$$

and boundary conditions

$$\begin{aligned} \mathbf{u}^\varepsilon &= \bar{\mathbf{u}}^\varepsilon \text{ on } \partial_u \Omega^\varepsilon, & \mathbf{n} \cdot \boldsymbol{\sigma}^\varepsilon &= \bar{\mathbf{h}}^\varepsilon \text{ on } \partial_\sigma \Omega^\varepsilon, \\ \partial_u \Omega^\varepsilon \cup \partial_\sigma \Omega^\varepsilon &= \partial \Omega^\varepsilon, & \partial_u \Omega^\varepsilon \cap \partial_\sigma \Omega^\varepsilon &= \emptyset, \end{aligned} \quad (3)$$

represent the non-linear problem, which is further linearized in the framework of the updated Lagrangian formulation. The linearized incremental form of the problem will be subjected to the homogenization procedure, resulting in a coupled system of macroscopic and microscopic equations. External volume forces \mathbf{f}^ε , surface tractions $\bar{\mathbf{h}}^\varepsilon$, whereby \mathbf{n} is the unit normal, and the prescribed displacements $\bar{\mathbf{u}}^\varepsilon$ are applied in a series of quasi-static loading steps.

2.1. Weak formulation

Following the procedure described in [5], we define the sets of admissible displacements

$$\mathbf{V}^\varepsilon \in \{\mathbf{v}^\varepsilon | \mathbf{v}^\varepsilon \in \mathbf{H}^1(\Omega^\varepsilon)^\varepsilon = \bar{\mathbf{u}}^\varepsilon \text{ on } \partial_u \Omega^\varepsilon\}, \quad \mathbf{V}_0^\varepsilon \in \{\mathbf{v}^\varepsilon | \mathbf{v}^\varepsilon \in \mathbf{H}^1(\Omega^\varepsilon)^\varepsilon = 0 \text{ on } \partial_u \Omega^\varepsilon\}, \quad (4)$$

respecting the boundary conditions (3). In the above definitions, sufficient regularity for unknown and test displacements is assumed. By $\mathbf{V}^\varepsilon(t)$, $\mathbf{V}_0^\varepsilon(t)$ we express the dependency on the spatial configuration $\Omega^\varepsilon(t)$. The weak form of the non-linear problem (1)-(3) for the unknown displacement field $\mathbf{u}^\varepsilon \in \mathbf{V}^\varepsilon$ is given by

$$\Phi_t(\mathbf{u}^\varepsilon, \mathbf{v}^\varepsilon) = \int_{\Omega^\varepsilon(t)} \boldsymbol{\sigma}(\mathbf{u}^\varepsilon) : \nabla \mathbf{v}^\varepsilon \, d\Omega - \int_{\Omega^\varepsilon(t)} \mathbf{f}^\varepsilon \cdot \mathbf{v}^\varepsilon \, d\Omega - \int_{\partial_\sigma \Omega^\varepsilon(t)} \bar{\mathbf{h}}^\varepsilon \cdot \mathbf{v}^\varepsilon \, dS = 0, \quad \forall \mathbf{v}^\varepsilon \in \mathbf{V}_0^\varepsilon(t), \quad (5)$$

where $\Phi_t(\mathbf{u}^\varepsilon, \mathbf{v}^\varepsilon)$ is the residual function evaluated at time t . In order to get the incremental formulation of the above problem a constant time step δt is assumed and the residual equation is rewritten at time $t + \delta t$ employing the first order Taylor expansion at time t ,

$$\Phi_{t+\delta t}(\mathbf{u}^\varepsilon(t + \delta t), \mathbf{v}^\varepsilon) \approx \Phi_t(\mathbf{u}^\varepsilon(t), \mathbf{v}^\varepsilon) + \delta \Phi_t(\mathbf{u}^\varepsilon(t), \mathbf{v}^\varepsilon) \circ (\delta \mathbf{u}^\varepsilon, \delta t \mathbf{V}). \quad (6)$$

Time increment $\delta \Phi_t(\mathbf{u}^\varepsilon(t), \mathbf{v}^\varepsilon) \circ (\delta \mathbf{u}^\varepsilon, \delta t \mathbf{V})$ appearing on the right-hand side of (6) is expressed in terms of displacement increment $\delta \mathbf{u}^\varepsilon$, defined such that $\mathbf{u}^\varepsilon(t + \delta t) \approx \mathbf{u}^\varepsilon(t) + \delta \mathbf{u}^\varepsilon = \mathbf{u}^\varepsilon(t) + \dot{\mathbf{u}}^\varepsilon \delta t$, and convection field \mathbf{V} , which is also used to approximate of the perturbed configuration of the domain: $\Omega^\varepsilon(t + \delta t) \approx \Omega^\varepsilon(t) + \delta t \mathbf{V}$, see [32, 5] for details. The differential of the residual function $\delta \Phi_t$ is further approximated by its total time derivative, so that

$$\begin{aligned} \delta \Phi_t \approx \delta t \dot{\Phi}_t = \delta t \left(\int_{\Omega^\varepsilon(t)} (\nabla \mathbf{V} \boldsymbol{\sigma}^\varepsilon + \mathcal{L}_{\mathbf{V}} \boldsymbol{\sigma}^\varepsilon) : \nabla \mathbf{v}^\varepsilon \, d\Omega \right. \\ \left. - \int_{\Omega^\varepsilon(t)} (\dot{\mathbf{f}}^\varepsilon \cdot \mathbf{v} + \mathbf{f}^\varepsilon \cdot \mathbf{v}^\varepsilon \nabla \cdot \mathbf{V}) \, d\Omega - \int_{\partial_\sigma \Omega^\varepsilon(t)} (\dot{\bar{\mathbf{h}}}^\varepsilon \cdot \mathbf{v}^\varepsilon + \bar{\mathbf{h}}^\varepsilon \cdot \mathbf{v}^\varepsilon \nabla \cdot \mathbf{V}) \, dS \right), \end{aligned} \quad (7)$$

where $\mathcal{L}_{\mathbf{V}} \boldsymbol{\sigma}^\varepsilon$ denotes the Lie derivative of the Cauchy stress tensor with respect to the convection field \mathbf{V} . This term can be expressed using the tangential stiffness operator \mathbf{D}^ε and the linear strain rate $\mathbf{e}(\dot{\mathbf{u}}^\varepsilon)$ as

$$\mathcal{L}_{\mathbf{V}} \boldsymbol{\sigma}^\varepsilon = \mathbf{D}^\varepsilon \mathbf{e}(\dot{\mathbf{u}}^\varepsilon). \quad (8)$$

The tangential fourth-order stiffness tensor \mathbf{D}^ε is the Truesdell rate of the Cauchy stress. For the compressible neo-Hookean material described by the stress-strain relation (1), it takes the form (see [33] and Appendix 8)

$$\begin{aligned} D_{ijkl}^\varepsilon = & K^\varepsilon (2J - 1) \delta_{ij} \delta_{kl} - K^\varepsilon (J - 1) (\delta_{ik} \delta_{lj} + \delta_{il} \delta_{jk}) \\ & + \mu^\varepsilon J^{-5/3} \left(\frac{2}{9} \text{tr}(\mathbf{b}) \delta_{ij} \delta_{kl} - \frac{2}{3} (b_{ij} \delta_{kl} + \delta_{ij} b_{kl}) + \frac{1}{3} \text{tr}(\mathbf{b}) (\delta_{ik} \delta_{lj} + \delta_{il} \delta_{jk}) \right). \end{aligned} \quad (9)$$

The prescribed displacements $\bar{\mathbf{u}}^\varepsilon$, volume forces \mathbf{f}^ε , and surface forces $\bar{\mathbf{h}}^\varepsilon$ are applied in a finite number of times steps $t_k = k \delta t$, $t = 0, 1, 2, \dots, N_t$ assuming a constant time step δt . Using this time discretization, the time derivative $\dot{\mathbf{u}}^\varepsilon$ appearing in (8) can be replaced by the forward finite difference,

$$\dot{\mathbf{u}}^\varepsilon(t_k) \approx (\mathbf{u}^{\varepsilon, (k+1)} - \mathbf{u}^{\varepsilon, (k)}) / \delta t = \delta \mathbf{u}^{\varepsilon, (k+1)} / \delta t, \quad (10)$$

and the velocity field $\mathbf{V}(t_k)$ can be approximated by the unknown displacement increment $\delta \mathbf{u}^{\varepsilon, (k+1)}$,

$$\mathbf{V}(t_k) \approx \delta \mathbf{u}^{\varepsilon, (k+1)} / \delta t. \quad (11)$$

Substituting (7)-(11) into equation (6) and with respect to the equilibrium (5) we get the following incremental formulation of the nonlinear problem: For a given Cauchy stress $\boldsymbol{\sigma}^{\varepsilon, (k)}$ and new loads $\mathbf{f}^{\varepsilon, (k+1)}$, $\bar{\mathbf{h}}^{\varepsilon, (k+1)}$ find displacement increments $\delta \mathbf{u}^{\varepsilon, (k+1)} \in \delta \mathbf{V}^\varepsilon$ ($\delta \mathbf{V}^\varepsilon$ is a set of admissible displacement increments) such that

$$\begin{aligned} \int_{\Omega^{\varepsilon, (k)}} \mathbf{A}^\varepsilon \nabla \delta \mathbf{u}^{\varepsilon, (k+1)} : \nabla \mathbf{v}^\varepsilon \, d\Omega = & - \int_{\Omega^{\varepsilon, (k)}} \boldsymbol{\sigma}^{(k)} : \nabla \mathbf{v}^\varepsilon \, d\Omega \\ & + \int_{\Omega^{\varepsilon, (k)}} \mathbf{f}^{(k+1)} \cdot \mathbf{v}^\varepsilon \, d\Omega + \int_{\partial_\sigma \Omega^{\varepsilon, (k)}} \bar{\mathbf{h}}^{(k+1)} \cdot \mathbf{v}^\varepsilon \, dS, \quad \forall \mathbf{v}^\varepsilon \in \mathbf{V}_0^\varepsilon(t). \end{aligned} \quad (12)$$

By $\Omega^{\varepsilon, (k)}$ we refer to the actual spatial configuration $\Omega^\varepsilon(t_k)$. The symmetric fourth-order tangent tensor \mathbf{A}^ε is defined as

$$A_{ijkl}^\varepsilon = D_{ijkl}^\varepsilon + \sigma_{jl}^\varepsilon \delta_{ik}. \quad (13)$$

Note that the incremental problem (12) still remains nonlinear due to the dependence of \mathbf{A}^ε on the current deformation state, and therefore must be solved in an iterative loop, e.g. by a Newton's method.

3. Two-scale model of locally periodic structures

The standard homogenization procedure is applied to the nonlinear incremental problem (12) to derive the limit model for $\varepsilon \rightarrow 0$, where the non-dimensional parameter ε defines the period size of the microstructure. The justification for applying two-scale homogenization to materials undergoing large deformations, and thus potentially losing periodicity, is discussed in detail in [5], Section 4, where the concepts of slowly varying microstructures and locally periodic media are introduced.

The heterogeneous material with a periodic structure can be characterized by a reference periodic cell Y , which may consist of several parts with different material properties. In the numerical examples presented in Section 7, we consider a two-phase microstructure composed of a compliant matrix with embedded stiffer inclusions, as illustrated in the left part of Figure 8.

The displacement increment in (12) can be expressed in the form of the truncated asymptotic expansion

$$\mathcal{T}_\varepsilon\left(\delta\mathbf{u}^{\varepsilon,(k+1)}\right) = \delta\mathbf{u}^0(x) + \varepsilon\delta\mathbf{u}^1(x, y) + O(\varepsilon^2), \quad x \in \Omega, \quad y \in Y, \quad (14)$$

where $\mathcal{T}_\varepsilon(\cdot)$ is the unfolding operator, see e.g. [4], $\delta\mathbf{u}^0(x)$ is the macroscopic displacement increment depending on x , and $\delta\mathbf{u}^1(x, y)$ is a two-scale function. The analogous expansion is used for the test function \mathbf{v}^ε . For the unfolded elastic tensor \mathbf{A}^ε and the terms at the r.h.s. of (12) the following expansions hold:

$$\begin{aligned} \mathcal{T}_\varepsilon(\mathbf{A}^\varepsilon) &= \tilde{\mathbf{A}}(x, y) + \varepsilon\mathbf{A}^*(x, y), \\ \mathcal{T}_\varepsilon\left(\boldsymbol{\sigma}^{\varepsilon,(k)}\right) &= \tilde{\boldsymbol{\sigma}}(x, y) + \varepsilon\boldsymbol{\sigma}^*(x, y) + O(\varepsilon^2), \\ \mathcal{T}_\varepsilon\left(\mathbf{f}^{\varepsilon,(k+1)}\right) &= \tilde{\mathbf{f}}(x, y) + O(\varepsilon), \\ \mathcal{T}_\varepsilon\left(\tilde{\mathbf{h}}^{\varepsilon,(k+1)}\right) &= \tilde{\mathbf{h}}(x, y) + O(\varepsilon). \end{aligned} \quad (15)$$

Substituting the expansion (14) into (12), taking into account $\nabla_y\delta\mathbf{u}^0(x) = \mathbf{0}$, and passing to the limit $\varepsilon \rightarrow 0$ yields

$$\begin{aligned} \int_{\Omega} \int_Y \tilde{\mathbf{A}}(\nabla_x\delta\mathbf{u}^0 + \nabla_y\delta\mathbf{u}^1) : (\nabla_x\mathbf{v}^0 + \nabla_y\mathbf{v}^1) \, dY \, d\Omega = \\ \int_{\Omega} \int_Y \tilde{\boldsymbol{\sigma}} : (\nabla_x\mathbf{v}^0 + \nabla_y\mathbf{v}^1) \, dY \, d\Omega + \int_{\Omega} \int_Y \tilde{\mathbf{f}} \cdot \mathbf{v}^0 \, dY \, d\Omega + \int_{\partial_\sigma\Omega} \int_Y \tilde{\mathbf{h}} \cdot \mathbf{v}^0 \, dY \, dS. \end{aligned} \quad (16)$$

Terms with tensors \mathbf{A}^* , $\boldsymbol{\sigma}^*$ vanish in the limit, see Eq. (58) and Section 4.4 in [5]. The integral \int_Y denotes the average value over the microscopic domain Y

$$\int_Y f \, dY = \frac{1}{|Y|} \int_Y f \, dY. \quad (17)$$

Recall that (16) is obtained from the weak form (12) of the linearized sub-problem associated with one load increment of the nonlinear problem arising from equilibrium (2). For each load increment, incorporating volume forces and the boundary tractions, the two-scale nonlinear problem is solved iteratively using corrections $(\delta\mathbf{u}^0, \delta\mathbf{u}^1)$ satisfying (16) with the right-hand side presenting the actual out-of-balance. Within one iteration called “outer” labelled by i , the couple $(\delta\mathbf{u}^0, \delta\mathbf{u}^1)$ is computed in the following steps which are described in detail below, in Sections 3.1–3.3.

1. **Step M0**: computing $\delta\mathbf{u}^0$ and updating the macro-configuration Ω , see Section 3.2;
2. **Step m1**: computing $\delta\mathbf{u}^1$ and updating the micro-configurations $Y(x)$, for $x \in \Omega$, see Section 3.3;
3. **Step m2**: updating the effective tangential (incremental) elasticity $\mathcal{A}(x)$ and effective Cauchy stress $\mathcal{S}(x)$ defined in (27), see Section 3.1.

Thus, the problem is decomposed into macroscopic subproblems for corrections $\delta\mathbf{u}_{[i]}^0$ in response to the out-of balance (iterations labelled by i), and the local “microproblems” which split into 2 steps: **Step m1** involves “inner” iterations $j = 0, 1, \dots$ associated with computing local equilibrium for given macroscopic strain – for a given global iteration i , a sequence of local micro-configurations $Y_{[i]}^{(j)}(x)$ is constructed, starting with $\tilde{Y}_{[i]}(x) = Y_{[i]}^{(0)}(x)$ which is given by virtue of the characteristic

response computed in $Y_{[i-1]}(x)$ for the preceding macroscopic iteration $i - 1$; **Step m2** consists in solving characteristic response to applied macroscopic strain increment modes. These steps are arranged in the computational scheme which is illustrated in Fig. 1.

Remark 1. From (16), the local problems are obtained for vanishing \mathbf{v}^0 , and testing by $\mathbf{v}^1 := \mathbf{v} \in \mathbf{H}_{\#}^1(Y)$, hence at almost all $x \in \Omega$,

$$\int_Y \tilde{\mathbf{A}}(\nabla_x \delta \mathbf{u}^0 + \nabla_y \delta \mathbf{u}^1) : \nabla_y \mathbf{v} \, dY = \int_Y \tilde{\boldsymbol{\sigma}} : \nabla_y \mathbf{v} \, dY, \quad \forall \mathbf{v} \in \mathbf{H}_{\#}^1(Y). \quad (18)$$

Assume the previous iteration $i-1$ yielding $\delta \mathbf{u}_{[i-1]}^0$ due to **Step M0**, which means also updating the local configuration $Y_{[i-1]}(x) \mapsto \tilde{Y}_{[i]}(x)$. Due to **Step m1**, the local equilibrium in (18) is achieved: let $\delta \mathbf{u}^1 = \delta \tilde{\mathbf{u}}^\sigma + \delta \tilde{\mathbf{u}}^1$, such that (18) can be written (at any $x \in \Omega$) as

$$\int_{\tilde{Y}_{[i]}} \tilde{\mathbf{A}}(\nabla_x \delta \mathbf{u}^0 + \nabla_y(\delta \tilde{\mathbf{u}}^1 + \delta \tilde{\mathbf{w}}^\sigma)) : \nabla_y \mathbf{v} \, dY = \int_{\tilde{Y}_{[i]}} \tilde{\boldsymbol{\sigma}} : \nabla_y \mathbf{v} \, dY, \quad \forall \mathbf{v} \in \mathbf{H}_{\#}^1(\tilde{Y}_{[i]}). \quad (19)$$

This problem is decomposed into two subproblems: Find $\delta \tilde{\mathbf{w}}^\sigma \in \mathbf{H}_{\#}^1(\tilde{Y}_{[i]})$, such that (we drop the macroscopic iteration index $[i]$)

$$\int_{\tilde{Y}} \tilde{\mathbf{A}} \nabla_y \delta \tilde{\mathbf{w}}^\sigma : \nabla_y \mathbf{v} \, dY = \int_{\tilde{Y}} \tilde{\boldsymbol{\sigma}} : \nabla_y \mathbf{v} \, dY, \quad \forall \mathbf{v} \in \mathbf{H}_{\#}^1(\tilde{Y}). \quad (20)$$

Using the solution $\delta \tilde{\mathbf{w}}^\sigma$, the micro-configuration is updated: $\tilde{Y} := \tilde{Y} + \delta \tilde{\mathbf{w}}^\sigma$ and the stress $\tilde{\boldsymbol{\sigma}}$ is computed using the actual deformation gradients (recall we consider a hyperelastic material). Problem (20) formulated in the updated configuration is solved repeatedly in iterations $j = 0, 1, \dots$ until the r.h.s. evaluated with the actual $\tilde{\boldsymbol{\sigma}}$ vanishes, i.e. until $\nabla_y \tilde{\boldsymbol{\sigma}} = 0$ in \tilde{Y} . In the schematic view of the whole algorithm, Fig. 1, the provisional micro-configurations $\tilde{Y} = Y_{[i]}^{(j)}$, are labelled by index j .

Then (19) considered in the actual local equilibrium configuration $Y_{[i]} := \tilde{Y}$ yields the linear problem: Given $\delta \mathbf{u}^0$, find $\delta \tilde{\mathbf{u}}^1 \in \mathbf{H}_{\#}^1(Y_{[i]})$, such that

$$\int_{Y_{[i]}} \tilde{\mathbf{A}}(\nabla_x \delta \mathbf{u}^0 + \nabla_y \delta \tilde{\mathbf{u}}^1) : \nabla_y \mathbf{v} \, dY = 0, \quad \forall \mathbf{v} \in \mathbf{H}_{\#}^1(Y_{[i]}). \quad (21)$$

This identity can be interpreted in the context of the two-scale limit (16), whereby $\delta \tilde{\mathbf{u}}^1 = \delta \mathbf{u}^1$, since the local configuration is in the local equilibrium, $\delta \tilde{\mathbf{w}}^\sigma = 0$, and the r.h.s. is presented by the macroscopic external forces only. By virtue of the linearity, the characteristic response can be introduced, which enables obtaining the homogenized elasticity coefficients. Consequently, the two-scale computational procedure proceeds with **Step M0**. Details are given below.

In subsequent sections, the three main steps embedded in the cycles associated with the “outer” and “inner” iterations are presented in a shifter order: **Step m2**, **Step M0** and **Step m1**.

3.1. Local microscopic problem – Step m2

By virtue of the linearity of the limit equations the fluctuating function $\delta \mathbf{u}^1$ can be decomposed in terms of the so called characteristic responses $\boldsymbol{\omega}^{ij}$ and the gradient of the macroscopic deformation $\nabla_x \delta \mathbf{u}^0$,

$$\delta \mathbf{u}^1 = \boldsymbol{\omega}^{ij} (\nabla_x \delta u_i^0)_j. \quad (22)$$

Taking $\mathbf{v}^0 = \mathbf{0}$ in (16) and using decomposition (22), the local problem for the unknown characteristic response can be defined: Find $\boldsymbol{\omega}^{ij} \in \mathbf{H}_{\#}^1(Y)$, $i, j = 1, 2, (3)$, satisfying

$$a_Y(\boldsymbol{\omega}^{ij} + \boldsymbol{\Pi}^{ij}, \mathbf{v}^1) = 0, \quad \forall \mathbf{v}^1 \in \mathbf{H}_{\#}^1(Y), \quad (23)$$

where $\Pi_k^{ij} = y_j \delta_{ik}$ and $a_Y(\mathbf{u}, \mathbf{v})$ is the bilinear form

$$a_Y(\mathbf{u}, \mathbf{v}) = \int_Y \tilde{\mathbf{A}} \nabla_y \mathbf{u} : \nabla_y \mathbf{v} \, dY. \quad (24)$$

The functional space $\mathbf{H}_{\#}^1(Y)$ denotes the standard Sobolev space of Y -periodic functions. Note that the integral in (24) is evaluated over the deformed microscopic configuration $Y = Y(x, t)$.

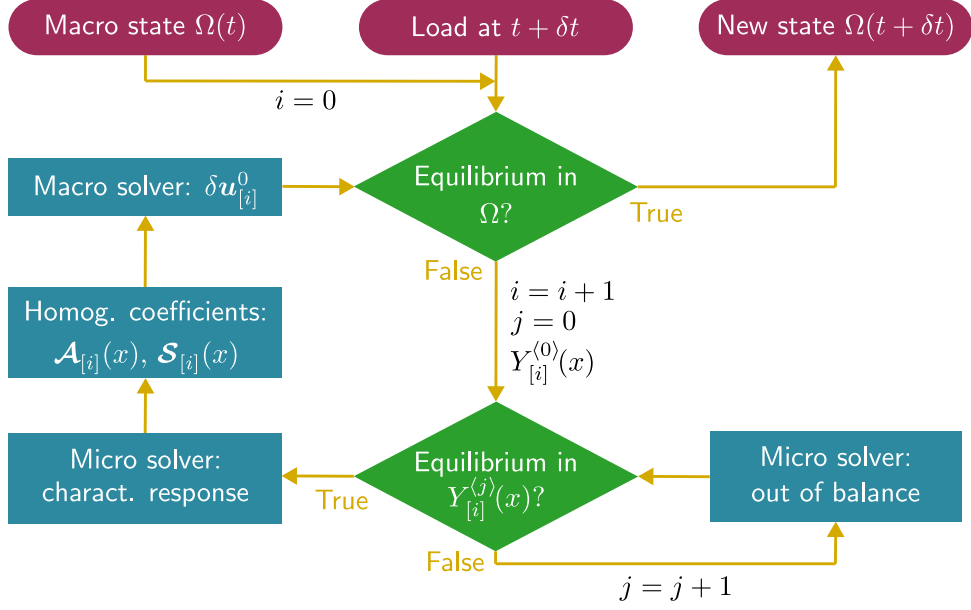


Figure 1: Inner/outer iterations within one “loading-time” step.

3.2. Global macroscopic problem and homogenized coefficients – Step $M0$

For the vanishing microscopic test functions $\mathbf{v}^1 = \mathbf{0}$ equation (16) results in

$$\int_{\Omega} \int_Y \tilde{\mathbf{A}} (\nabla_x \delta \mathbf{u}^0 + \nabla_y \delta \mathbf{u}^1) : \nabla_x \mathbf{v}^0 dY d\Omega = \int_{\Omega} \int_Y \tilde{\boldsymbol{\sigma}} : \nabla_x \mathbf{v}^0 dY d\Omega + \int_{\Omega} \int_Y \tilde{\mathbf{f}} \cdot \mathbf{v}^0 dY d\Omega + \int_{\partial_\sigma \Omega} \int_Y \tilde{\mathbf{h}} \cdot \mathbf{v}^0 dY dS, \quad (25)$$

Substituting the decomposition (22) into (25), the macroscopic equilibrium problem can be formulated as follows: For given volume and surface forces included in $L^{\text{new}}(\mathbf{v}^0)$ and homogenized coefficients \mathbf{A} , \mathbf{S} , find the macroscopic displacement increments $\delta \mathbf{u}^0 \in \delta \mathbf{V}(\Omega)$ such that

$$\int_{\Omega} \mathbf{A} \nabla_x \delta \mathbf{u}^0 : \nabla_x \mathbf{v}^0 d\Omega = L^{\text{new}}(\mathbf{v}^0) - \int_{\Omega} \mathbf{S} : \nabla_x \mathbf{v}^0 d\Omega, \quad \forall \mathbf{v}^0 \in \mathbf{V}_0(\Omega). \quad (26)$$

The homogenized elastic tensor \mathbf{A} and averaged Cauchy stress tensor \mathbf{S} can be identified from (25) as:

$$\begin{aligned} \mathcal{A}_{ijkl} &= a_Y (\boldsymbol{\omega}^{kl} + \mathbf{\Pi}^{kl}, \boldsymbol{\omega}^{ij}) = a_Y (\boldsymbol{\omega}^{kl} + \mathbf{\Pi}^{kl}, \boldsymbol{\omega}^{ij} + \mathbf{\Pi}^{ij}), \\ \mathbf{S} &= \int_Y \tilde{\boldsymbol{\sigma}} dY, \end{aligned} \quad (27)$$

see [34, 5] for details.

3.3. Update microscopic configurations – Step $m1$

The solution of the microscopic subproblems and the evaluation of the coefficients at a given macroscopic point $x \in \Omega$ must be performed on a update microscopic configurations $Y(x)$ following the evolution of the macroscopic deformation $\delta \mathbf{u}^0$. The updating procedure is illustrated in Fig. 2 and can be expressed as

$$\begin{aligned} \delta \mathbf{w} &= (\boldsymbol{\omega}^{ij} + \mathbf{\Pi}^{ij}) (\nabla_x \delta u_i^0)_j \\ \tilde{Y}(x) &:= Y(x) + \{\delta \mathbf{w}\}. \end{aligned} \quad (28)$$

The stress $\tilde{\boldsymbol{\sigma}}$ updated due to (28) does not automatically satisfy the microscopic equilibrium, so

$$\nabla_y \cdot \tilde{\boldsymbol{\sigma}} \neq \mathbf{0}. \quad (29)$$

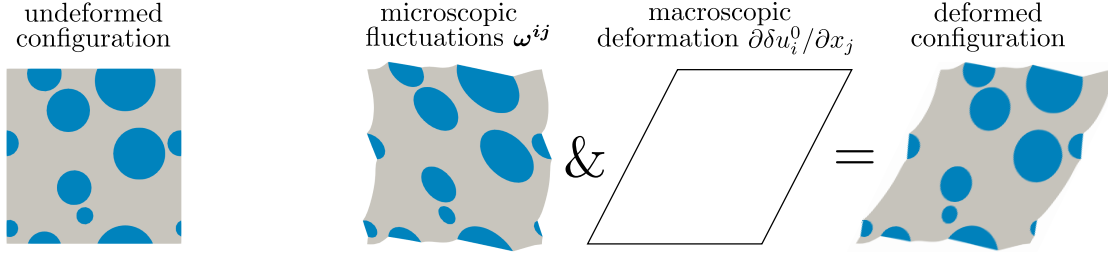


Figure 2: Updating microscopic configurations using the characteristic responses and ω^{ij} and the gradient of the macroscopic displacement increments $\delta \mathbf{u}^0$.

To ensure the local equilibrium (i.e. for all local configurations $\tilde{Y}(x)$, $x \in \Omega$), as explained in Remark 1, see problem (20), corrections $\delta \mathbf{w} \in \mathbf{H}_{\#}^1(Y^{(j)})$ are computed in iterations $j = 0, 1, \dots$ by solving

$$a_{Y^{(j)}}(\delta \mathbf{w}^{j+1}, \mathbf{v}) = - \int_{Y^{(j)}} \tilde{\boldsymbol{\sigma}} : \nabla_y \mathbf{v} \, dY, \quad \forall \mathbf{v} \in \mathbf{H}_{\#}^1(Y^{(j)}), \quad (30)$$

where $Y^{(j+1)} = Y^{(j)} + \{\delta \mathbf{w}^{j+1}\}$ and $Y^{(0)} = \tilde{Y}$ according to (28)₂.

3.4. Sensitivities of homogenized coefficients

The approximation scheme for efficient computing of the deformation dependent homogenized coefficients proposed in Section 4 employs the coefficient sensitivities $\delta \mathcal{A}$ and $\delta \mathcal{S}$ that are introduced in this section.

Based on the shape sensitivity theory and on the domain parametrization technique (see [35] and Appendix 8), the following sensitivity of the bilinear form $a_Y(\mathbf{u}, \mathbf{v})$ holds

$$\begin{aligned} \delta_{\tau} a_Y(\mathbf{u}, \mathbf{v}) &= \int_Y \tilde{A}_{irks} (\delta_{rj} \delta_{sl} \nabla_y \cdot \boldsymbol{\nu} - \delta_{jr} \partial_s^y \nu_l - \delta_{ls} \partial_r^y \nu_j) \partial_l^y u_k \partial_j^y v_i \, dY \\ &\quad + \int_Y \delta \tilde{\mathbf{A}} \nabla_y \mathbf{u} : \nabla_y \mathbf{v} \, dY - a_Y(\mathbf{u}, \mathbf{v}) \int_Y \nabla_y \cdot \boldsymbol{\nu} \, dY, \end{aligned} \quad (31)$$

cf. [36] or [37], where the similar formulae for a piezoelectric medium are derived. With (31) in hand, employing the abbreviation $\Xi^{ij} = \omega^{ij} + \Pi^{ij}$, and introducing $\delta_{\tau} \Pi_k^{ij} = \nu_j \delta_{ik}$, the sensitivity expression for the elastic tensor can be defined,

$$\delta \mathcal{A}_{kl ij} = \delta_{\tau} a_Y(\Xi^{ij}, \Xi^{kl}) + a_Y(\delta_{\tau} \Pi^{ij}, \Xi^{kl}) + a_Y(\Xi^{kl}, \delta_{\tau} \Pi^{kl}). \quad (32)$$

For the sensitivity of the averaged Cauchy stress, the following expression holds:

$$\delta \mathcal{S} = \int_Y (\tilde{\boldsymbol{\sigma}} - \mathcal{S}) \nabla_y \cdot \boldsymbol{\nu} \, dY + \int_Y \delta \tilde{\boldsymbol{\sigma}} \, dY. \quad (33)$$

Note that the first integral, recalling \mathcal{S} is constant in Y , describes the sensitivity of the stress inhomogeneous on the volumetric change of the RVE (cell Y), whereas the second one is the sensitivity of the local stress in Y . Details upon derivation of (32) and (33) are given in Appendix 8.

The sensitivity of the homogenized coefficients with respect to the components of the macroscopic deformation $(\nabla_x \delta u_i^0)_j$ is obtained by substituting $\Pi^{ij} + \omega^{ij}$ for the velocity field $\boldsymbol{\nu}$ in (32) and (33). The derivatives $\delta \tilde{\boldsymbol{\sigma}}$, $\delta \tilde{\mathbf{A}}$ are computed employing relations (58) and (62).

4. Approximation of homogenized coefficients

Solving the nonlinear macroscopic problem using the finite element method requires computing the deformation-dependent tangent moduli and stress tensors at all quadrature points of the discretized macroscopic domain. The tangent moduli and stresses are associated with the solutions of the local microscopic subproblems (23), and the computation must be repeated at every iteration of the nonlinear algorithm. This approach, commonly referred to as FE², is highly computationally demanding even for relatively simple 2D problems. To avoid the computational bottleneck

of the FE² method, we propose a novel algorithm, CSA (“Clustering and Sensitivity based Approximation”), that reduces the number of solved local subproblems. Our approach leverages the K-means clustering method to group macroscopic deformations and employs sensitivity analysis to approximate the homogenized coefficients efficiently.

Let $\{\hat{x}^i\} \subset \Omega$, $i = 1, \dots, \hat{N}$, be the set of all macroscopic quadrature points where the homogenized coefficients $\mathcal{A}(\hat{x})$ and $\mathcal{S}(\hat{x})$, which depend on the macroscopic deformation $\mathbf{F}(\hat{x})$, must be evaluated. The first step of our algorithm involves performing the polar decomposition of the deformation gradient $\mathbf{F}(\hat{x})$ into the rotation tensor $\hat{\mathbf{R}}$ and the symmetric stretch tensor $\hat{\mathbf{U}}$,

$$\mathbf{F}(\hat{x}) = \hat{\mathbf{R}}\hat{\mathbf{U}}. \quad (34)$$

The deformation state of the microstructure is fully characterized by the symmetric strain tensor $\mathbf{e}(\hat{x}) = \hat{\mathbf{e}} = \hat{\mathbf{U}} - \mathbf{I}$, as the rotation tensor $\hat{\mathbf{R}}$ does not influence the local response. The components of $\hat{\mathbf{e}}$ can be interpreted as coordinates of a point in \mathbb{R}^3 for 2D problems or \mathbb{R}^6 for 3D problems, and the proximity of two deformation states can be quantified using the L^2 norm.

The key aspect of the proposed approach is to find the minimal number \hat{N} of sets O^j , $j = 1, \dots, \hat{N}$, such that their union $\bigcup_{j=1}^{\hat{N}} O^j$ covers all current macroscopic strains $\hat{\mathbf{e}}$:

$$O^j = \{\hat{\mathbf{e}} : |\hat{\mathbf{e}} - \hat{\mathbf{e}}^j| < \rho\}, \quad \{\hat{\mathbf{e}}\} \subset \bigcup_{j=1}^{\hat{N}} O^j, \quad (35)$$

where $\hat{\mathbf{e}}^j$ denotes the mean value (center) of the strains in O^j , $|\hat{\mathbf{e}}|$ is the Euclidean norm in \mathbb{R}^3 or in \mathbb{R}^6 respectively, and ρ is a given parameter. The sets O^j may overlap, allowing a single strain value to belong to multiple sets, which can improve the accuracy of the coefficients approximation. Among the various strategies for finding the minimal number of sets O^j , we adopt the K-means clustering method [38], as suggested in [28]. Throughout this paper, the sets O^j are referred to as centroids.

Instead of solving the local microscopic subproblems for all \hat{N} macroscopic deformations $\mathbf{e}(\hat{x}^i)$, we solve them now only for a reduced number of deformations $\hat{\mathbf{e}}^j$, $j = 1, \dots, \hat{N}$, to obtain the corresponding homogenized coefficients $\hat{\mathcal{A}}^j$ and $\hat{\mathcal{S}}^j$. The number of centroids \hat{N} may increase dynamically during the macroscopic iterations whenever newly occurring strains cannot be classified into the existing centroids.

To approximate the coefficients $\mathcal{A}(\hat{x})$ and $\mathcal{S}(\hat{x})$ at the quadrature points \hat{x} , we compute not only $\hat{\mathcal{A}}$ and $\hat{\mathcal{S}}$, but also their sensitivities $\delta\hat{\mathcal{A}}$, $\delta\hat{\mathcal{S}}$ with respect to deformations. This computation is efficient, as the sensitivities depend only on the already computed correctors $\boldsymbol{\omega}$, see Section 3.4 and [34]. Given all coefficients $\hat{\mathcal{A}}^j$, $\hat{\mathcal{S}}^j$ and their sensitivities $\delta\hat{\mathcal{A}}^j$, $\delta\hat{\mathcal{S}}^j$, coefficients $\mathcal{A}(\hat{x}^i)$, $\mathcal{S}(\hat{x}^i)$ at any quadrature point \hat{x}^i can be approximated as

$$\begin{aligned} \mathcal{A}_{klmn}(\hat{x}^i) &\approx \hat{R}_{kp}^i \hat{R}_{lq}^i \hat{R}_{mr}^i \hat{R}_{ns}^i \hat{\mathcal{A}}_{pqrs}^i, & \tilde{\mathcal{A}}^i &= \sum_{l \in \mathcal{I}^i} \left(\hat{\mathcal{A}}^l + \delta\hat{\mathcal{A}}^l \circ \mathbf{g}^{il} \right) w^{il}, \\ \mathcal{S}_{kl}(\hat{x}^i) &\approx \hat{R}_{kp}^i \hat{R}_{lq}^i \hat{\mathcal{S}}_{pq}^i, & \tilde{\mathcal{S}}^i &= \sum_{l \in \mathcal{I}^i} \left(\hat{\mathcal{S}}^l + \delta\hat{\mathcal{S}}^l \circ \mathbf{g}^{il} \right) w^{il}, \end{aligned} \quad (36)$$

where the index set \mathcal{I}^i is defined by $j \in \mathcal{I}^i \Leftrightarrow \hat{x}^i \in O^j$, so that the sum runs over all centroids containing $\hat{\mathbf{e}}^i$. The weights w^{il} are introduced to ensure a smooth approximation when centroids overlap:

$$w^{il} = d^{il} / \sum_{m \in \mathcal{I}^i} d^{im}, \quad d^{il} = (\rho - |\hat{\mathbf{e}}^i - \hat{\mathbf{e}}^l|)^2, \quad \sum_{l \in \mathcal{I}^i} w^{il} = 1, \quad (37)$$

The relative deformation \mathbf{g}^{il} appearing in (36) represents the deformation of $\hat{\mathbf{e}}^i$ with respect to the centroid $\hat{\mathbf{e}}^l$ and is defined using the multiplicative decomposition, yielding

$$\mathbf{g}^{il} = (\hat{\mathbf{e}}^i + \mathbf{I})(\hat{\mathbf{e}}^l + \mathbf{I})^{-1} - \mathbf{I}. \quad (38)$$

Figure 3 illustrates the weight calculation for the case of three overlapping centroids.

The deformed microstructures $\mathbf{Y}(\hat{\mathbf{e}}^i)$ associated with the macroscopic deformation states $\hat{\mathbf{e}}^i$ are obtained by

$$\hat{\mathbf{y}}^i \approx \left(\sum_{l \in \mathcal{I}^i} \left(\hat{\mathbf{y}}^l + \hat{\boldsymbol{\Xi}}^{rs,l} g_{rs}^{il} \right) w^{il} \right) \hat{\mathbf{R}}^i, \quad (39)$$

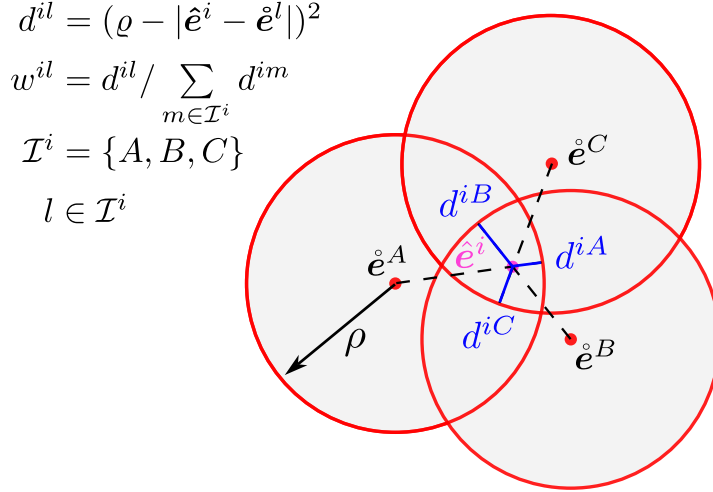


Figure 3: Calculation of weights w^{il} for the case of three overlapping centroids.

where $\hat{\mathbf{y}}^l$ are the coordinates of the configuration $Y(\hat{\mathbf{e}}^l)$, and $\hat{\mathbf{y}}^i$ define $Y(\hat{\mathbf{e}}^i)$.

To evaluate the difference between the approximated coefficients given by (36) and those obtained from the direct numerical solution of (23), a test was performed on a single periodic cell subjected to macroscopic uniaxial strain. The periodic cell, whose geometry and material composition are specified in Section 7, was gradually loaded by the varying macroscopic strain $\mathbf{e} = [e_{11}, 0, 0]$, for $e_{11} \in (0, 0.015)$. Two different strategies were employed to approximate the coefficients between two overlapping centroids $O^1 = O([0, 0, 0], 0.01)$ and $O^2 = O([0.015, 0, 0], 0.01)$, both of size $\rho = 0.01$. The first strategy uses the coefficient sensitivities $\delta \hat{\mathcal{A}}, \delta \hat{\mathcal{S}}$ and is represented by the blue solid curve “CSA” in Figure 4. The second strategy relies solely on the values $\hat{\mathcal{A}}, \hat{\mathcal{S}}$ in O_1 and O_2 (setting $\delta \hat{\mathcal{A}} = \mathbf{0}, \delta \hat{\mathcal{S}} = \mathbf{0}$ in (36)) and its results are plotted in Figure 4 by the red dashed curve “CnoSA”. Both approximations are compared with the direct two-scale simulation denoted by “FE²” in graphs. The computations in Fig. 4 were performed for a relatively large centroid size ρ to demonstrate the properties of the proposed approximation. The corresponding results for smaller centroids, $O^1 = O([0, 0, 0], 0.001)$ and $O^2 = O([0.0015, 0, 0], 0.001)$ with $\rho = 0.001$, are presented in Figure 5.

5. Computational algorithm for reduced two-scale simulation

At the beginning of the two-scale simulation, the macroscopic configuration is undeformed, so that $\mathbf{F}(\hat{\mathbf{x}}^i) = \mathbf{I}$ at all quadrature points $\hat{\mathbf{x}}^i, i = 1, \dots, \hat{N}$. In this initial state, the microscopic problem is solved for a single centroid $O^1 = O(\mathbf{0}, \rho)$, and the homogenized coefficients $\hat{\mathcal{A}}(\hat{\mathbf{x}}^i), \hat{\mathcal{S}}(\hat{\mathbf{x}}^i)$ are constant across the macroscopic domain. As the macroscopic domain deforms, some strains get out of the existing centroid, and the K-mean clustering algorithm is invoked to generate the minimal number of new centroids required to cover all strains $\hat{\mathbf{e}}^i$. The microscopic subproblems are then solved only for those strains $\hat{\mathbf{e}}$ corresponding to the newly created centroids. Finally, based on the values calculated for centroids, the homogenized coefficients are evaluated for all quadrature points. These steps are repeated at each iteration of the macroscopic solution.

The procedure of centroid creation is illustrated in Fig. 6, where the deformation space is represented by two dimensions for clarity, however it is three dimensional for 2D problems. Fig. 6a depicts the initial state, while Fig. 6b and 6c show two subsequent iterations. Assume that at the k -th macroscopic iteration (Fig. 6b) all strains $\hat{\mathbf{e}}^i$ from previous iterations are covered by centroids $O^j, j = 1, \dots, \hat{N}^{(k)}$, which are associated with the deformed microscopic configurations \hat{Y}^j and coefficients $\hat{\mathcal{A}}^j, \hat{\mathcal{S}}^j, \delta \hat{\mathcal{A}}^j, \delta \hat{\mathcal{S}}^j$. In the $(k+1)$ -th iteration (Fig. 6c), new strains $\hat{\mathbf{e}}^{i,(k+1)}$ arise due to the updated macroscopic state. Some of these strains may fit in the existing $\hat{N}^{(k)}$ centroids, while others require the creation of \hat{N}^{new} additional centroids to satisfy (35). For these new centroids $O^{\hat{N}+l}, l = 1, \dots, \hat{N}^{new}$, microscopic subproblems must be solved on the deformed configurations \hat{Y}^l to evaluate coefficients $\hat{\mathcal{A}}^l, \hat{\mathcal{S}}^l, \delta \hat{\mathcal{A}}^l, \delta \hat{\mathcal{S}}^l$.

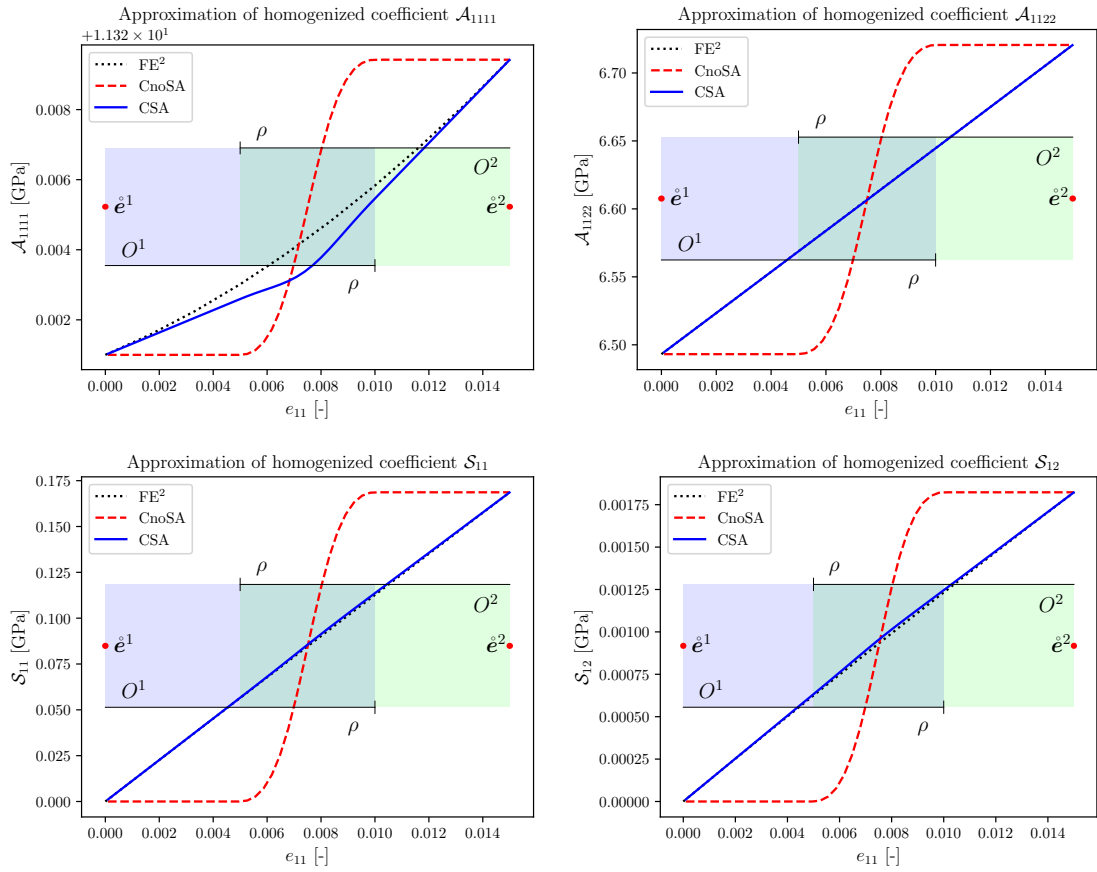


Figure 4: Approximations of \mathcal{A} , \mathcal{S} between two centroids $O^1 = O([0, 0, 0], 0.01)$, $O^2 = O([0.015, 0, 0], 0.01)$ with $\rho = 0.01$. Comparison of the direct two-scale simulation (FE²) – black dotted line, approximation using coefficients sensitivities (CSA) – blue solid line, and approximation without sensitivity information (CnoSA, $\delta\mathcal{A} = \mathbf{0}$, $\delta\mathcal{S} = \mathbf{0}$) – red dashed curve.

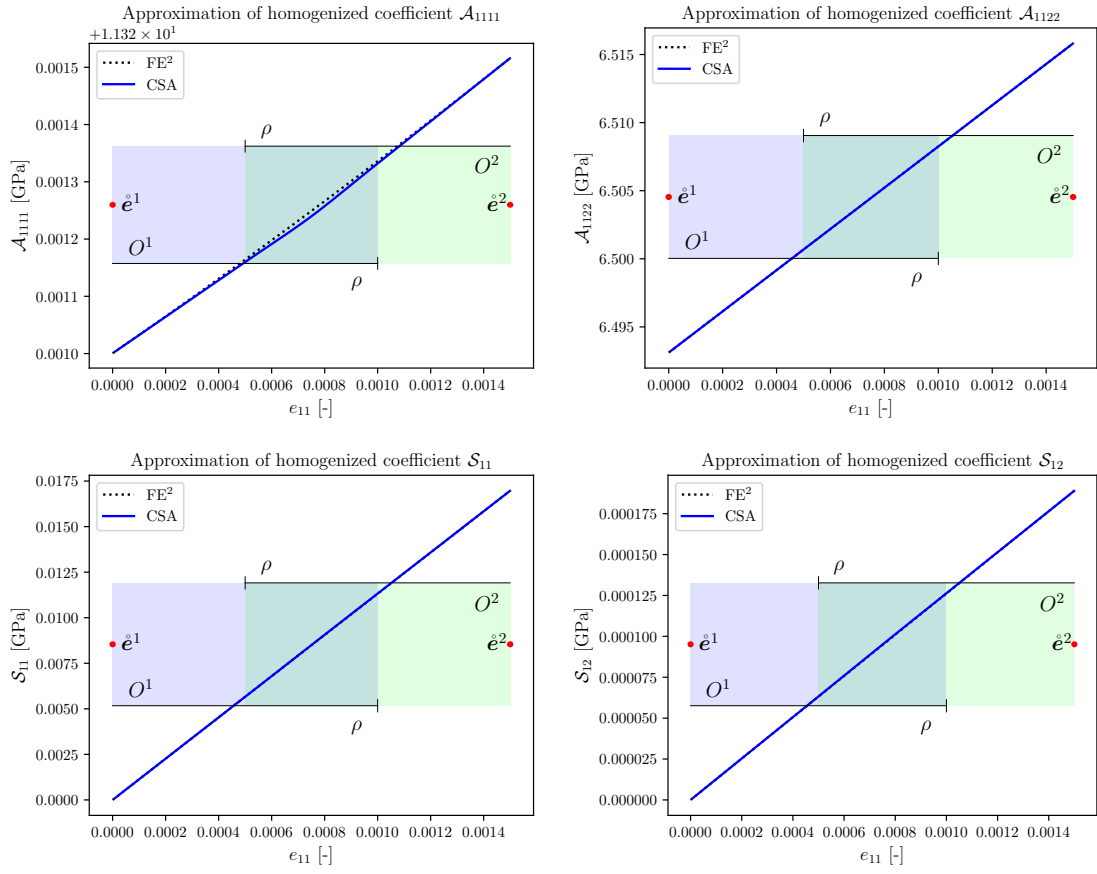


Figure 5: Approximations of \mathcal{A} , \mathcal{S} between two centroids $O^2 = O([0, 0, 0], 0.001)$, $O^1 = O([0.0015, 0, 0], 0.001)$ with $\rho = 0.001$. Comparison of the direct numerical simulation (FE²) – black dotted line and approximation using coefficients sensitivities (CSA) – blue solid line.

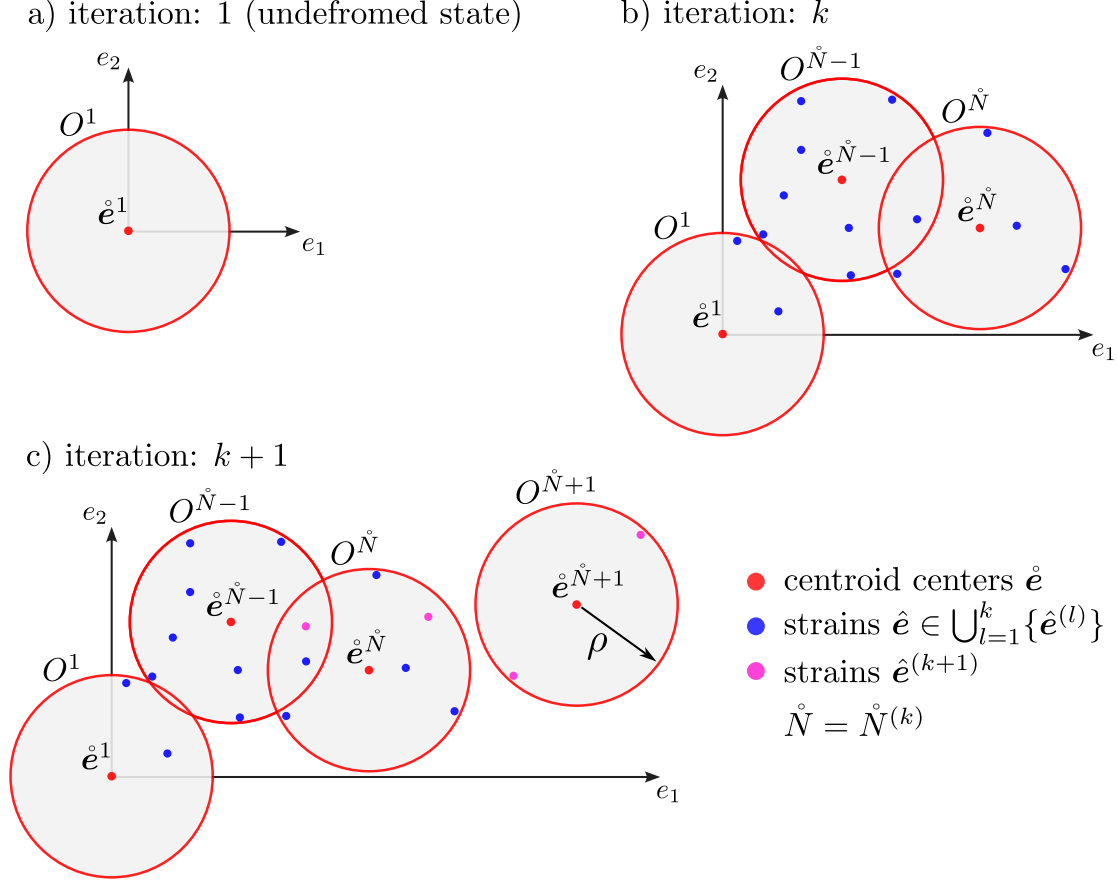


Figure 6: Creation of new centroids: a) initial centroid associated with the undefromed macroscopic state b) centroids in the k -th iteration c) a new centroid created in the $(k+1)$ -th iteration to cover all strains $\hat{e}^{(k+1)}$.

Due to the nonlinear behavior of the microstructure, the deformed configurations $\hat{Y}^l = Y(\hat{e}^l)$ cannot be obtained by a “jump” deformations \hat{e}^l but must be reached incrementally to maintain equilibrium at the microscopic level. To achieve this efficiently, the closest existing configuration $\hat{Y}^m = Y(\hat{e}^m)$,

$$m = \arg \min_{i \in \{1, \dots, \dot{N}^{(k)}\}} |\hat{e}^i - \hat{e}^l|, \quad (40)$$

is selected as a reference, and the update from \hat{Y}^m to \hat{Y}^l is done via (28), where $\nabla_x \mathbf{u}^0$ is replaced by the relative deformation \mathbf{g}^{lm} defined in (38).

The computational procedure for the reduced two-scale simulation is summarize in Algorithms 1, 2, and 3. Replacing CSA_COEFS_APPROX function with FE2_COEFS function (defined in Algorithms 4) in Algorithm 1 yields the full FE² computational scheme.

6. Model reduction using proper orthogonal decomposition

To assess the efficiency of the proposed CSA approach against a well-established technique, we implemented the R3M algorithm described in [17], which is based on the proper orthogonal decomposition (POD) method [39] applied to the microscopic subproblems. The R3M method constructs a reduced basis from precomputed solutions of the microscopic problem corresponding to various macroscopic deformation states. This basis is then used to project the discretized microscopic problem onto a reduced-order model of significantly lower dimensionality, resulting in a substantial reduction of computational cost.

Discretization of the microscopic systems (23) and (30) by means of the finite element method leads to a system of discrete equations,

$$\mathbf{K}_\# \mathbf{q} = \mathbf{f}_\#, \quad (41)$$

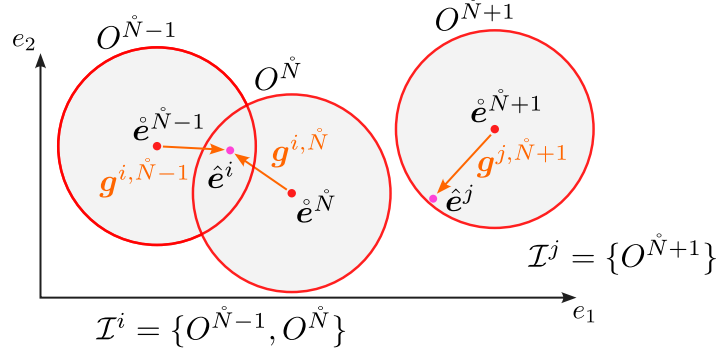


Figure 7: Illustration of homogenized coefficients approximation at points \hat{e}^i and \hat{e}^j , index sets \mathcal{I}^i , \mathcal{I}^j , and relative strains \mathbf{g}^{il} , \mathbf{g}^{jm} , where $l \in \mathcal{I}^i$, $m \in \mathcal{I}^j$.

Algorithm 1 Reduced two-scale nonlinear simulation – MACRO

function MACRO
 initial configuration:
 $\Omega^{(0)}, Y^{(0)}, \mathbf{u}^{0,(0)} := \mathbf{0}, \dot{N} := 0$

for time steps $k = 0, \dots, N_t - 1$ **do**
 given: $\Omega^{(k)}, \mathbf{u}^{0,(k)}$, load $\mathbf{f}_{ext}^{(k+1)}$
 $\mathbf{u}^{0,(k+1)} := \mathbf{u}^{0,(k)}, i := 1$

do
 calculate homogenized coefficients:
 $\mathcal{S}, \mathcal{A} = \text{CSA_COEFS_APPROX}(\nabla_x \mathbf{u}^{0,(k+1)})$

solve (26) for displacement increments $\delta \mathbf{u}^{0,(k+1),i}$
 update displacements: $\mathbf{u}^{0,(k+1)} := \mathbf{u}^{0,(k+1)} + \delta \mathbf{u}^{0,(k+1),i}$
 evaluate residue: $R := |\mathbf{f}_{ext}^{(k+1)} - \mathbf{f}_{int}^{(k,i)}|$
 $i := i + 1$

while $R > \epsilon_M$

step increment: $\delta \mathbf{u}^{0,(k+1)} = \mathbf{u}^{0,(k+1)} - \mathbf{u}^{0,(k)}$
 update macroscopic state: $\Omega^{(k+1)} := \Omega^{(k)} + \{\delta \mathbf{u}^{0,(k+1)}\}$

end for
end function

Algorithm 2 Reduced two-scale simulation – CSA_COEFS_APPROX

function CSA_COEFS_APPROX($\nabla_x \mathbf{u}$)
 $E := \emptyset$
 for $i = 1, \dots, \hat{N}$ **do**
 get $\hat{\mathbf{U}}^i, \hat{\mathbf{R}}^i$ from polar decomposition: $\mathbf{F}(\hat{x}^i) = \mathbf{I} + \nabla_x \mathbf{u}(\hat{x}^i) = \hat{\mathbf{R}}^i \hat{\mathbf{U}}^i$
 get symmetric strain tensor: $\hat{\mathbf{e}}^i = \hat{\mathbf{U}}^i - \mathbf{I}$
 if $\hat{\mathbf{e}}^i \notin \bigcup_{j=1}^{\hat{N}} O^j$ **then**
 $E := E \cup \{\hat{\mathbf{e}}^i\}$
 end if
 end for

 using *K-mean* method, create \hat{N}^{new} new centroids such that
 $E \subset \bigcup_{j=1}^{\hat{N}^{new}} O^{\hat{N}+j}$

 for $l = (\hat{N} + 1), \dots, (\hat{N} + \hat{N}^{new})$ **do**
 if $\hat{N} > 0$ **then:**
 find the closest centroid O^m to O^l
 evaluate relative deformation: \mathbf{g}^{lm}
 solve microscopic subproblem:
 $\hat{\mathcal{S}}^l, \hat{\mathcal{A}}^l, \delta \hat{\mathcal{S}}^l, \delta \hat{\mathcal{A}}^l, \hat{Y}^l, \hat{\omega}^{rs,l} = \text{MICRO}(\mathbf{g}^{lm}, \hat{Y}^m, \hat{\omega}^{rs,m})$
 else
 solve microscopic subproblem:
 $\hat{\mathcal{S}}^l, \hat{\mathcal{A}}^l, \delta \hat{\mathcal{S}}^l, \delta \hat{\mathcal{A}}^l, \hat{Y}^l, \hat{\omega}^{rs,l} = \text{MICRO}(\mathbf{0}, \hat{Y}^{(0)}, \mathbf{0})$
 end if
 $\hat{N} := \hat{N} + \hat{N}^{new}$
 end for

 for $i = 1, \dots, \hat{N}$ **do**
 approximate coefficients $\mathcal{S}(\hat{x}^i), \mathcal{A}(\hat{x}^i)$ using $\hat{\mathcal{S}}, \hat{\mathcal{A}}, \delta \hat{\mathcal{S}}, \delta \hat{\mathcal{A}}, \hat{\mathbf{R}}^i$
 end for

 return \mathcal{S}, \mathcal{A}
end function

Algorithm 3 Reduced two-scale nonlinear simulation – MICRO

function MICRO($\mathbf{g}, Y, \omega^{rs}$)
 evaluate: $\delta \mathbf{w} = (\mathbf{\Pi}^{rs} + \omega^{rs}) g_{rs}$
 update configuration: $Y^{\text{NEW}} := Y + \{\delta \mathbf{w}\}$

 do
 solve nonlinear problem (29) for corrections $\delta \mathbf{w}$
 update configuration: $Y^{\text{NEW}} := Y^{\text{NEW}} + \{\delta \mathbf{w}\}$
 evaluate residue: $R := |\delta \mathbf{w}|$
 while $R > \epsilon_{\#}$

 solve (23) for new characteristic responses $\omega^{rs, \text{NEW}}$
 evaluate: $\mathcal{S}, \mathcal{A}, \delta \mathcal{S}, \delta \mathcal{A}$

 return $\mathcal{S}, \mathcal{A}, \delta \mathcal{S}, \delta \mathcal{A}, Y^{\text{NEW}}, \omega^{rs, \text{NEW}}$
end function

Algorithm 4 Two-scale nonlinear simulation – FE2_COEFS

```

function FE2_COEFS( $\nabla_x \delta \mathbf{u}$ )
  for  $i = 1, \dots, \hat{N}$  do
     $\mathcal{S}(\hat{x}^i), \mathcal{A}(\hat{x}^i), Y(\hat{x}^i), \boldsymbol{\omega}^{rs}(\hat{x}^i) = \text{MICRO}(\nabla_x \delta \mathbf{u}(\hat{x}^i), Y(\hat{x}^i), \boldsymbol{\omega}^{rs}(\hat{x}^i))$ 
  end for

  return  $\mathcal{S}, \mathcal{A}$ 
end function
  
```

which is solved iteratively due to dependence of the tangent matrix $\mathbf{K}_\#$ on the total deformation. Vector \mathbf{q} of dimension $N_\#$ represents the characteristic responses $\boldsymbol{\omega}^{ij}$ or microscopic corrections $\delta \mathbf{w}$ after finite element discretization, where $N_\#$ denotes the number of degrees of freedom of the microscopic subproblem. To construct the reduced basis, the microscopic problem (41) is solved for a series of deformed configurations governed by the macroscopic strain

$$(\epsilon^{pqR})_{rs}(k) = k/(N_t - 1)\epsilon^{pqR}\delta_{pr}\delta_{qs}, \quad \text{for } k = 0, \dots, N_t - 1, \quad p, q = 1, 2, (3), \quad R = \min, \max, \quad (42)$$

where $\epsilon^{pq, \min}, \epsilon^{pq, \max}$ are the estimated minimum and maximum values of the strain components p, q , and N_t is a given number of load steps. For each load case $\alpha = pqR$, N_t solutions $\mathbf{q}^\alpha(k)$ of (41) are calculated and collected in matrix \mathbf{U}^α ,

$$\mathbf{U}^\alpha = [\mathbf{q}^\alpha(0), \mathbf{q}^\alpha(1), \dots, \mathbf{q}^\alpha(N_t - 1)]. \quad (43)$$

Matrices \mathbf{U}^α are further collected in $\mathbf{V} = [\mathbf{U}^{11, \min}, \mathbf{U}^{11, \max}, \dots, \mathbf{U}^{33, \max}]$ and the eigenvalue problem

$$\mathbf{V}\mathbf{V}^T \boldsymbol{\phi}_m = \lambda_m \boldsymbol{\phi}_m \quad (44)$$

is solved for the eigenvectors $\boldsymbol{\phi}_m$ and eigenvalues λ_m . The eigenvectors corresponding to the first $M(\delta)$ largest eigenvalues form the reduced orthogonal basis $\boldsymbol{\Phi} = [\boldsymbol{\phi}_1, \dots, \boldsymbol{\phi}_M]$ where M is chosen according to a given tolerance error parameter δ

$$\frac{\left(\sum_{l=M+1}^{N_\#} \lambda_l\right)^{1/2}}{\left(\sum_{l=1}^{N_\#} \lambda_l\right)^{1/2}} < \delta, \quad (45)$$

see [17] for details.

Using the pre-calculated basis $\boldsymbol{\Phi}$, the following approximation for correctors \mathbf{q} is used:

$$\mathbf{q} = \sum_{m=1}^M \boldsymbol{\phi}_m \xi_m = \boldsymbol{\Phi} \boldsymbol{\xi}. \quad (46)$$

Substituting (46) into (41), the reduced discrete system of dimensions $M \times M$ for the unknown multipliers $\boldsymbol{\xi}$ is obtained,

$$\boldsymbol{\Phi}^T \mathbf{K}_\# \boldsymbol{\Phi} \boldsymbol{\xi} = \boldsymbol{\Phi}^T \mathbf{f}_\#. \quad (47)$$

Since $Mp \ll N_\#$, the solution of (47) exhibits a substantially lower computational complexity compared to the full-order problem (41). This gain in the ‘‘on-line’’ phase is partially offset by the computational cost associated with the solution of a large-scale eigenvalue problem for the dense correlation matrix $\mathbf{V}\mathbf{V}^T$ of dimension $N_\# \times N_\#$. The efficiency of the reduced basis construction could be further improved through various approaches, e.g. by adopting more effective sampling strategies for the macroscopic deformation space, such as Latin hypercube sampling. A detailed discussion of these improvements is beyond the scope of the present work.

7. Numerical simulations

The coupled two-scale numerical simulations have been carried out using the *SfePy* package – Simple Finite Elements in Python, [40]. As its name suggests, the package implements the finite element (FE) method in Python and provides useful tools for the efficient realization of coupled

Part	shear modulus μ [GPa]	bulk modulus K [GPa]
matrix (epoxy) Y_m	1.35	5.7
inclusions (glass) Y_c	28.46	43.21

Table 1: Material properties of the compressible neo-Hookean hyperelastic structure.

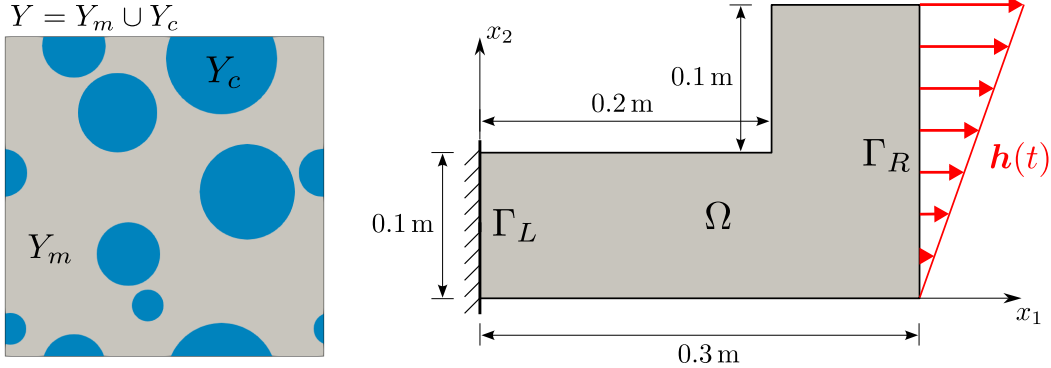


Figure 8: Left: decomposition of the microscopic reference cell $Y = Y_m \cup Y_c$; Right: undeformed macroscopic domain Ω and applied boundary conditions.

or uncoupled multiscale simulations, see [30]. The source code used to perform the computations presented in this paper is published in the Mendeley Data repository [31].

All subsequent simulations concern a two-dimensional problem of a heterogeneous periodic structure composed of two hyperelastic materials with distinct stiffness: a soft “matrix” and stiffer “inclusions”. The material parameters are summarized in Table 1. The periodic structure is represented by a reference unit cell $Y = Y_m \cup Y_c$, where Y_m denotes the soft matrix and Y_c the stiff inclusions. The undeformed configuration of the unit cell is shown in Fig. 8 left. At the macroscopic level, an L-shaped sample is fixed on its left hand side, $\mathbf{u}^0 = \mathbf{0}$ on Γ_L , and subjected to a surface traction on the opposite side, $\bar{\mathbf{h}} = \bar{\mathbf{h}}(x, t)$ on Γ_R . The traction is applied incrementally in $N_t = 10$ equal loading steps, see Figure 8 right,

$$\bar{\mathbf{h}}(x, t_k) = \begin{bmatrix} 10^8 r_k x_2 / 0.2 \\ 0 \end{bmatrix} \text{ N/m, for } r_k = \frac{k}{N_t - 1}, \quad t_k = r_k \cdot 1\text{s, and } k = 0, \dots, N_t - 1. \quad (48)$$

The displacement fields at both scales are approximated by the Lagrangian piece-wise linear elements and the nonlinear systems defined by (26) and (23) are solved using the Newton-Raphson iterative scheme. Since the macroscopic FE mesh consists of 36 quadrilateral elements, see Fig. 9 (left), and a four-point quadrature rule is used for numerical integration in all simulations, 36×4 deformation-dependent homogenized coefficients must be evaluated in each macroscopic iteration independently of the employed method (FE², CSA, or POD). In Sections 7.1 and 7.2, the reference cell Y is represented by a FE mesh (denoted as micro-mesh #1 in Tab. 2) consisting of 4166 triangular elements and 2160 nodes. In Section 7.3, several microscopic FE meshes with different levels of refinement are employed to study the effect of mesh density on computational time.

Section 7.1 presents the results of the reduced two-scale simulation and shows some numerical aspects of centroid formation. In Section 7.3, the computational efficiency of the proposed algorithm is evaluated and compared with the proper orthogonal decomposition approach briefly described in Sec. 6. The approximation error is analyzed in Section 7.2. The application of the CSA algorithm for a three dimensional case is demonstrated in Section 7.4.

7.1. Reduced micro-macro simulation

Running the coupled micro-macro simulation for N_t loading steps yields the deformed macroscopic sample depicted in Fig. 9 (left). The time evolution of the displacements at point D is plotted in Fig. 9 (right), where the nonlinear response to the linearly applied load arises from the nonlinear kinematics and hyperelastic material behavior. Figure 10 shows the components of the Green strain (left) and the averaged Cauchy stress (right) at the end of the simulation.

The reconstructed microstructures at three different points, A, B, and C, corresponding to the quadrature points of the macroscopic sample, are depicted in Fig. 11. The evolution of the homogenized coefficients \mathcal{A} , \mathcal{S} at these points during the loading steps is plotted in Figure 12.

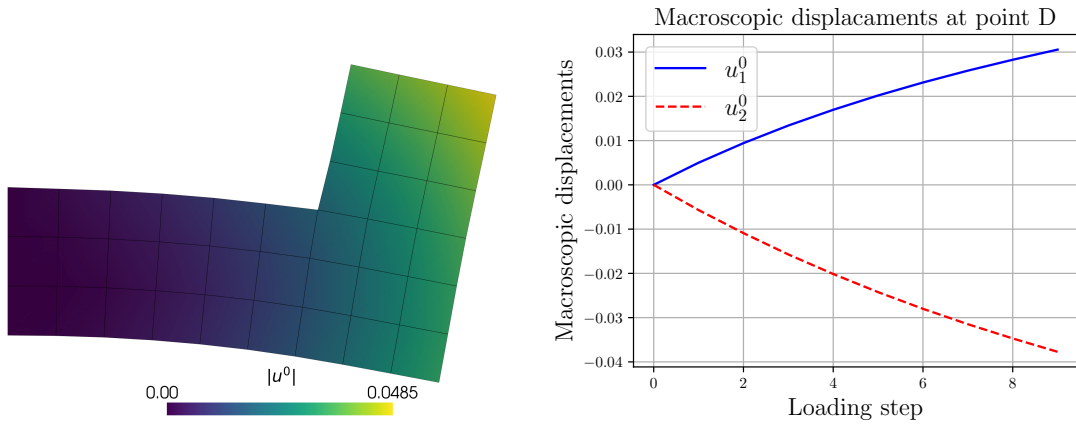


Figure 9: Left: resulting deformation in the last time step; Right: macroscopic displacements at point D.

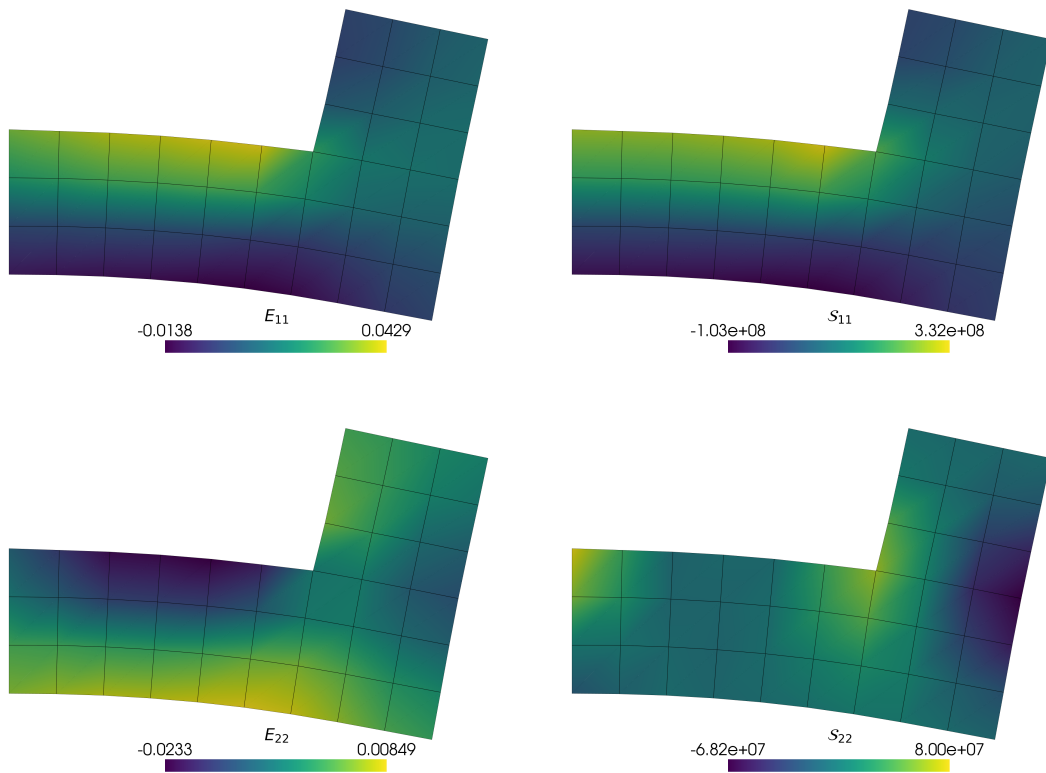


Figure 10: Left: components of the Green strain tensor; Right: components of the averaged Cauchy stress \mathcal{S} .

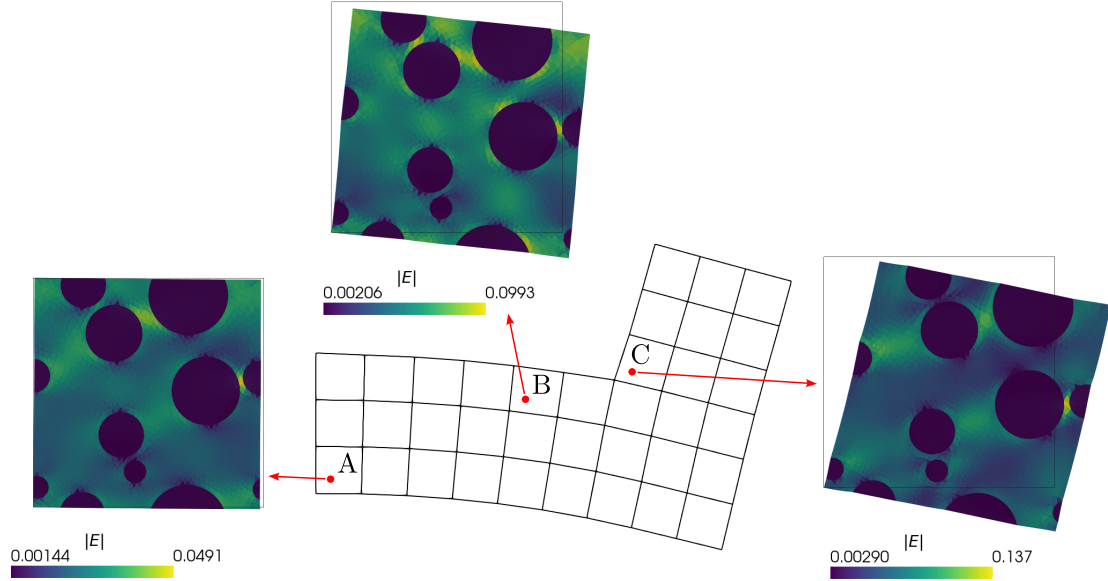


Figure 11: Reconstructed microstructures in the last loading step at quadrature points A, B, and C.

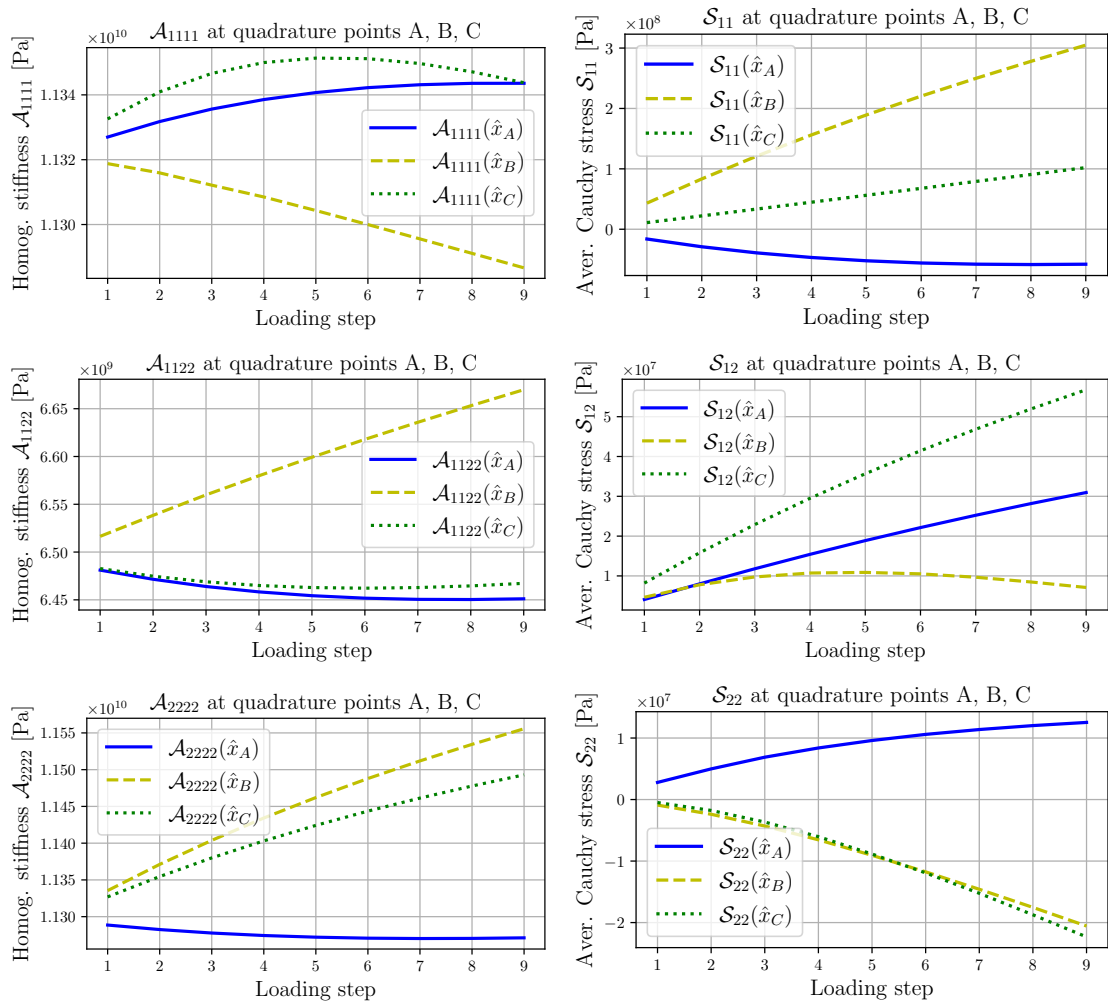


Figure 12: Evolution of the homogenized coefficients \mathcal{A} (left) and \mathcal{S} (right) at macroscopic quadrature points A, B, C.

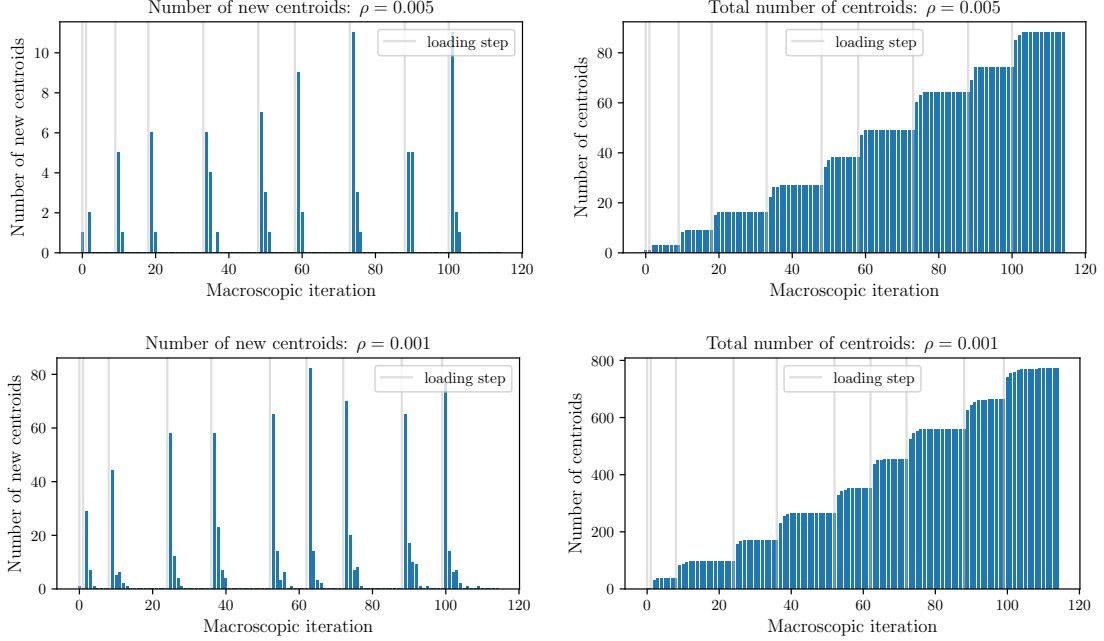


Figure 13: The number of new centroids in each macroscopic iteration step for $\rho = 0.005$ (top) and $\rho = 0.001$ (bottom).

As described in Sec. 4, centroids are generated dynamically as the deformation progresses due to external loading. The number of new centroids at each iteration step is shown in Fig. 13 (left), while the total (cumulative) number of centroids created throughout the simulation is presented in Fig. 13 (right). The results are shown for two centroid sizes $\rho = 0.005$ (top) and $\rho = 0.001$ (bottom).

The homogenized coefficients at the quadrature points of the macroscopic domain are approximated using the values and sensitivities evaluated at one or more centroids. If the deformation associated with a quadrature point \hat{x}^i belongs to a single centroid O^l , the index set \mathcal{I}^i reduces to l , the corresponding weight w^{il} equals 1, and (36) yields an extrapolation from \mathcal{A}^l , \mathcal{S}^l to $\mathcal{A}(\hat{x}^i)$, $\mathcal{S}(\hat{x}^i)$. When the deformation lies within multiple centroids, the homogenized coefficients are obtained by interpolation according to (36), using the weights defined in (37). The number of centroids approximating the coefficients for $\rho = 0.005$ in the final iterations of time steps 1 and 9 is shown in the upper part of Figure 14. To display the which cluster is employed to approximate the homogenized coefficients, the finite elements are subdivided into four sub-parts each comprising one integration point, according to the use of the four-point integration scheme. The lower part of Fig. 14 shows the number of macroscopic quadrature points for which the coefficients are approximated using values from one, two, three, or four centroids. At load step 1, the coefficients at approximately 55% of the quadrature points are obtained by extrapolation from a single centroid, while those at the remaining points are determined by interpolation between two or three centroids.

7.2. Approximation error

To test the accuracy of the approximated homogenized coefficients, the relative and cumulative errors are defined as

$$Err_{\mathcal{S}_{ij}^k}^{rel}(\hat{x}) = \frac{|\mathcal{S}_{ij}^{k,CSA}(\hat{x}) - \mathcal{S}_{ij}^{k,FE^2}(\hat{x})|}{|\mathcal{S}_{ij}^{k,FE^2}(\hat{x})|}, \quad (49)$$

$$Err_{\mathcal{S}_{ij}^k}^{cum}(\hat{x}) = \sum_k^{N_{iter}} Err_{\mathcal{S}_{ij}^k}^{rel}(\hat{x})$$

where $\mathcal{S}^{CSA}(\hat{x})$ is the approximated coefficient obtained from (36), and $\mathcal{S}^{FE^2}(\hat{x})$ is the direct numerical solution of the microscopic problem, both evaluated for the same macroscopic deformation $\mathbf{F}(\hat{x})$. The superscript k denotes the k -th macroscopic iteration, and \hat{x} is the position of the quadrature point. Analogous definitions apply to the homogenized elastic coefficient \mathcal{A} .

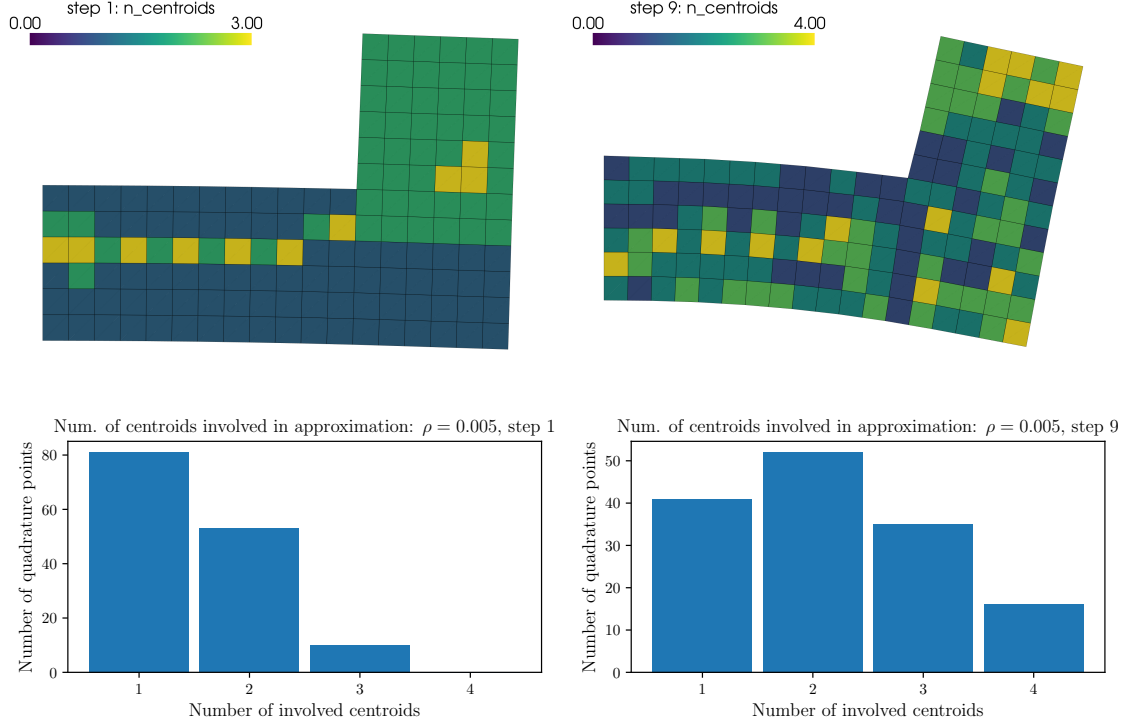


Figure 14: The number of centroids approximating the coefficients for $\rho = 0.005$ in the final iterations of time steps 1 (left) and 9 (right).

Figure 15 shows the evolution of the relative errors of \mathcal{A}_{1111} , \mathcal{A}_{2222} , \mathcal{S}_{11} , and \mathcal{S}_{22} at two selected quadrature points A and C (see Fig. 11), for the centroid size $\rho = 0.01, 0.005, 0.001, 0.0005$. The results indicate that the approximation error decreases as the centroid size ρ becomes smaller. For $\rho \approx 10^{-3}$, the relative error of \mathcal{S} is on the order of 10^{-3} and error of \mathcal{A} on the order of 10^{-5} . Insufficient accuracy for $\rho = 0.01$ leads to convergence issues at the macroscopic level, manifested as oscillations of the approximated coefficients encountered between consecutive iterations. These oscillations require the simulation to be terminated after reaching the maximum number of macroscopic iterations. During such oscillatory behavior, no new centroids are usually created, and the approximation of the coefficients is based solely on the existing centroids. The convergence of the approximated coefficients toward the directly computed values is more clearly illustrated in Figure 16, which shows the cumulative error as a function of ρ .

7.3. Time complexity of reduced calculations

The practical applicability of the proposed approximation method is determined by its accuracy, which was addressed in the previous section, as well as the computational efficiency it offers. In the proposed algorithm, the simulation time is influenced by the parameter ρ , which controls the approximation error, and by the finite element mesh resolution at both the macroscopic and microscopic scales. Since the number of macroscopic quadrature points is held constant for all simulations in this paper, our focus is restricted to the number of FE nodes and elements of the microscopic reference cell. To evaluate the computational complexity of the method, a series of FE microscopic meshes with identical geometry but varying numbers of elements and nodes were generated, see Table 2.

Figure 17 presents the solution time and the number of solved microproblems for micro-mesh #1 as functions of the centroid size ρ , compared to the direct numerical simulation. As seen in Fig 17 (left), the solution time exceeds that of the direct simulation as $\rho \rightarrow 10^{-4}$ due to the additional computational overhead associated with centroid generation, coefficient approximation, and the evaluation of coefficient sensitivities. With the increasing number of nodes in the microscopic FE mesh, the cost of solving the microscopic problems becomes dominant relative to the overhead, resulting in more significant computational savings provided by the proposed method. This trend is evident in Fig. 18 (left), where the relative solution time is defined as the ratio between the

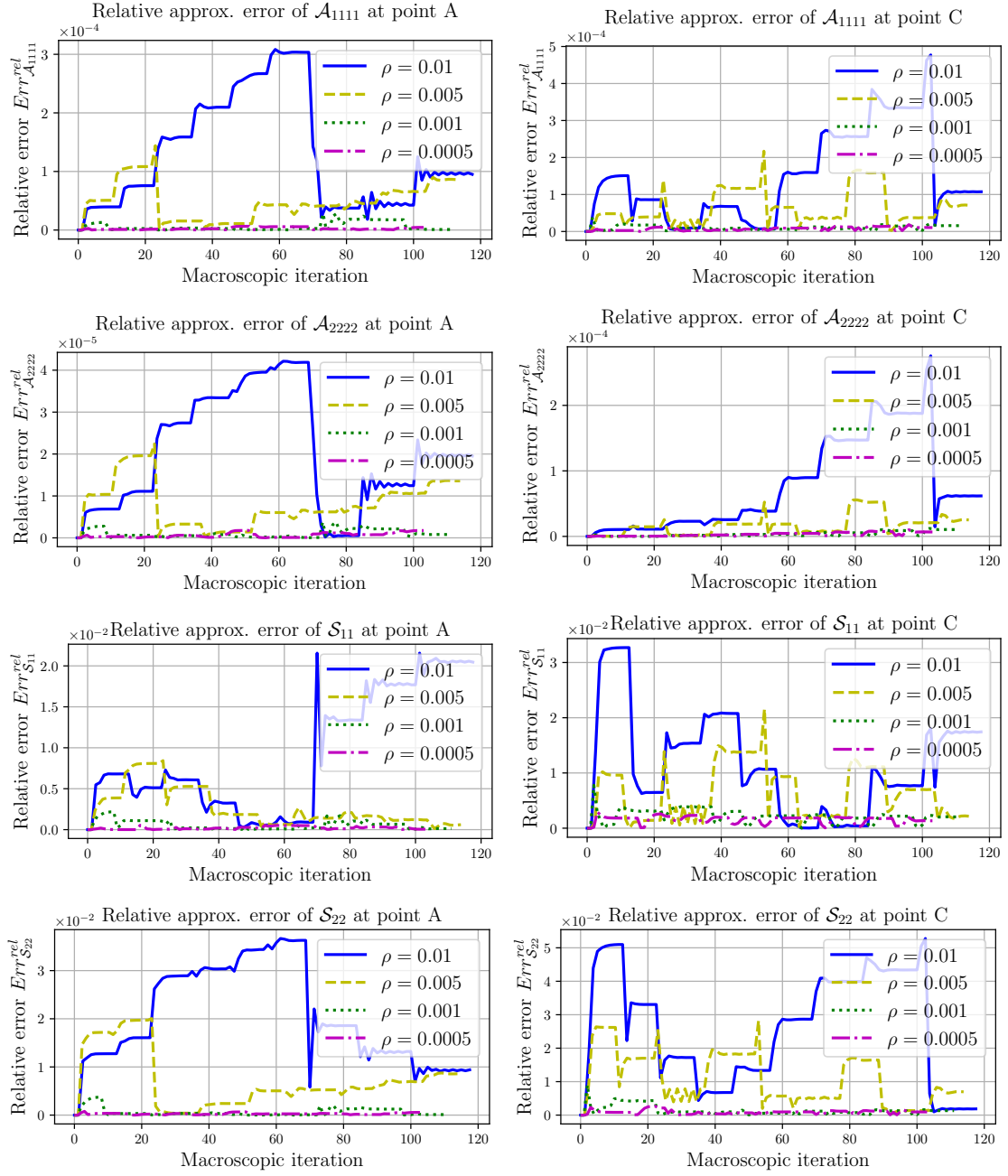


Figure 15: Relative errors of the homogenized coefficients at two quadrature points A (left) and C (right) calculated for the centroid size $\rho = 0.01, 0.005, 0.001, 0.0005$.

Micro-mesh ID	Num. elements	Num. nodes	
#1	4166	2160	
#2	15024	7961	
#3	24430	12399	
#4	42752	21620	
#5	57182	28872	

Table 2: Periodic reference cells with varying mesh density.

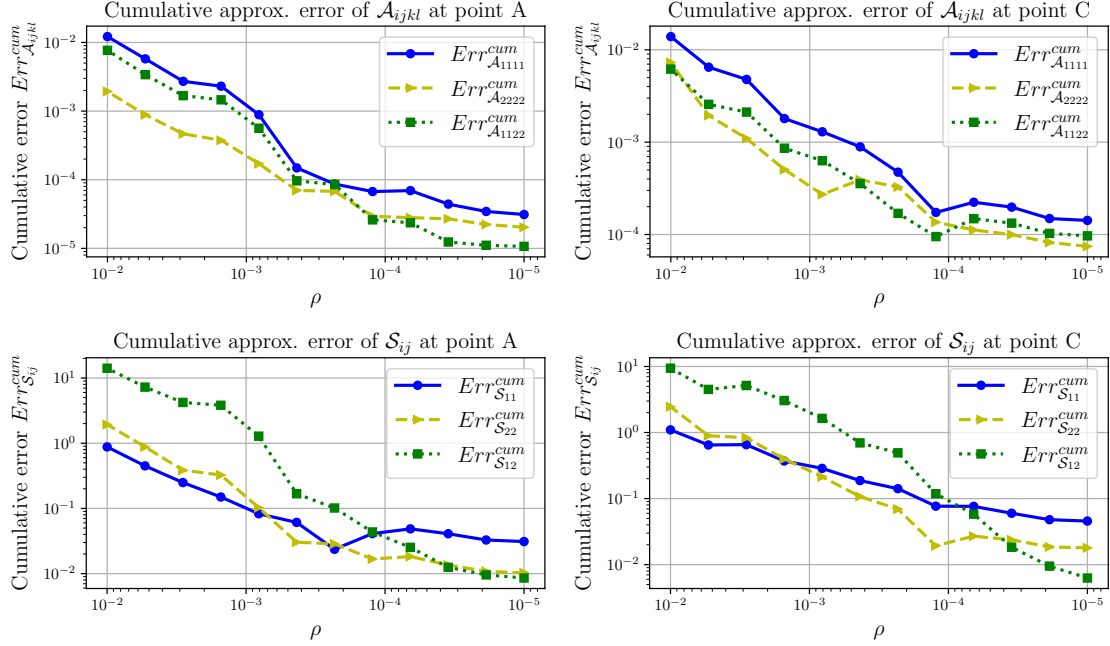


Figure 16: Cumulative error of coefficients \mathbf{A} , \mathbf{S} as a function of ρ .

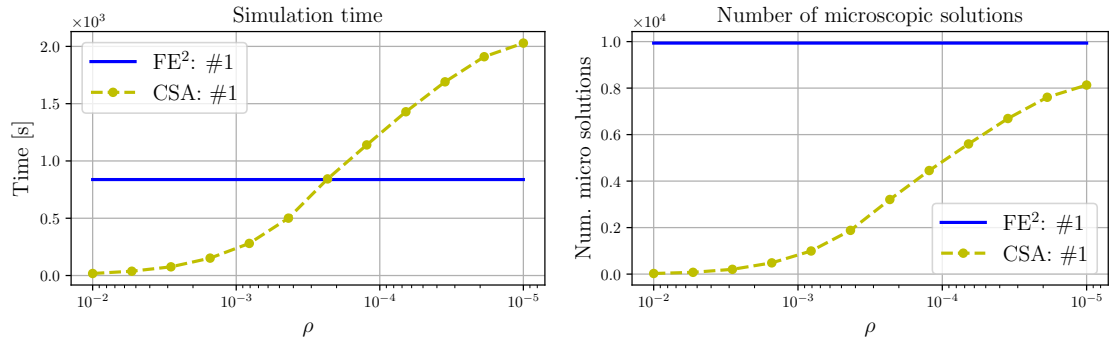


Figure 17: Solution time and number of solved microproblems for micro-mesh #1 as functions of ρ .

computational time of the reduced model and the direct simulation. The absolute simulation time as a function of the microscopic mesh size are presented in Fig. 18 (right).

When the local subproblems (23) are solved using a direct sparse linear solver, the total computational complexity for the coefficient evaluation is of order $o(N_{mac} \cdot N_{\#} \cdot b^2)$ [41] for both the FE² and CSA simulations, where $N_{\#}$ denotes the number of microscopic degrees of freedom, N_{mac} is the number of local subproblems, and b is the bandwidth of the sparse matrix arising from the FE discretization of the microscopic problem. For the FE², N_{mac} equals the number of macroscopic quadrature points multiplied by the number of macroscopic iterations, whereas for CSA, N_{mac} represents the number of centroids generated during the simulation. Since N_{mac} remains constant for a given algorithm and b does not change with varying mesh density, the overall time complexity exhibits linear scaling behavior, as confirmed in Fig. 18 (right).

The efficiency of the CSA algorithm is compared against the direct simulation and the proper orthogonal decomposition method, see [17], in Fig. 19. In the figure, “POD” refers to the simulation time using a pre-computed orthogonal basis and “POD – basis calc.” denotes the time required for computing that basis. The POD simulations are carried out with the error parameter $\delta = 0.02$, and the CSA simulations use the centroid size $\rho = 0.0005$. These settings yield a comparable order of the macroscopic error measured by $Err_{\mathbf{u}_D^0}^{rel}$, as illustrated in Fig. 20, where

$$Err_{\mathbf{u}_D^0}^{rel}(x_D) = \frac{|\mathbf{u}^{0,CSA}(x_D) - \mathbf{u}^{0,FE^2}(x_D)|}{|\mathbf{u}^{0,FE^2}(x_D)|}. \quad (50)$$

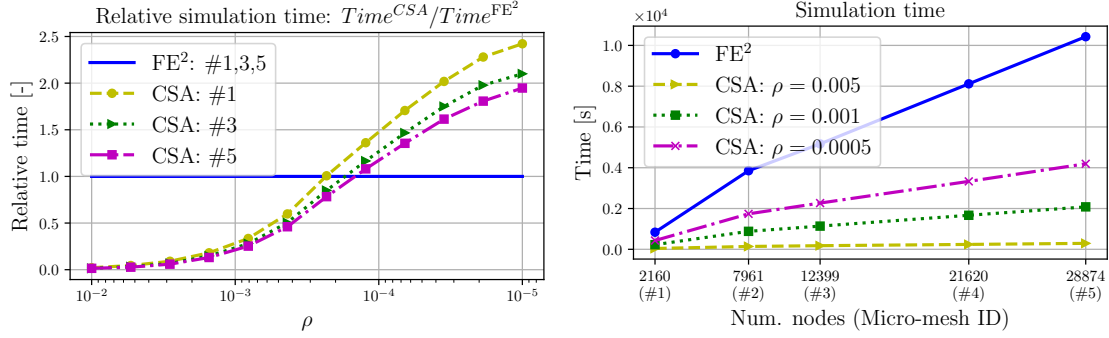


Figure 18: Left: relative simulation time as a function of ρ for various microscopic FE mesh size; Right: simulation time as a function of microscopic FE mesh size.

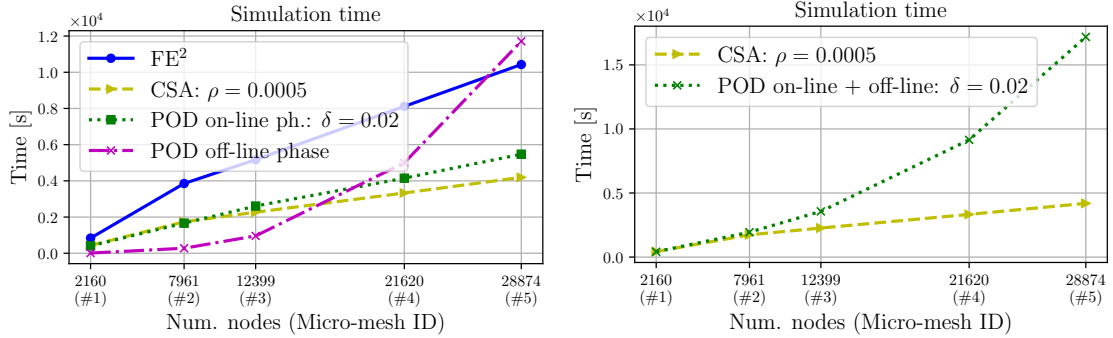


Figure 19: Comparison of the simulation times of the proposed reduction algorithm (for $\rho = 0.0005$), direct simulation, and the POD method ($\delta = 0.02$).

The complexity of the POD “on-line” phase is primarily given by the solution of the reduced (dense) system (47) of dimension $M \times M$, which is independent of $N_{\#}$, and by the matrix multiplications required for order reduction. These operations show linear time complexity scaling, as demonstrated in Fig. 19 by the green dotted line. In contrast, the “off-line” phase involves solving the eigenvalue problem (44) for a dense symmetric matrix of dimension $N_{\#} \times N_{\#}$ with complexity of order $o(N_{\#}^3)$, as shown by the cyan dash-dotted line in Fig. 19. This cubic growth can considerably limit the applicability of the POD for very large microscopic FE meshes.

All numerical simulations were implemented in the general-purpose FE package *SfePy* [30] without any significant optimization. Using dedicated, highly optimized implementations of individual algorithms would likely result in shorter simulation times.

7.4. 3D example

The implementation of the CSA algorithm in *SfePy* also enables solution of three-dimensional problems, as demonstrated in this section. At the macroscopic level, a block-shaped specimen with

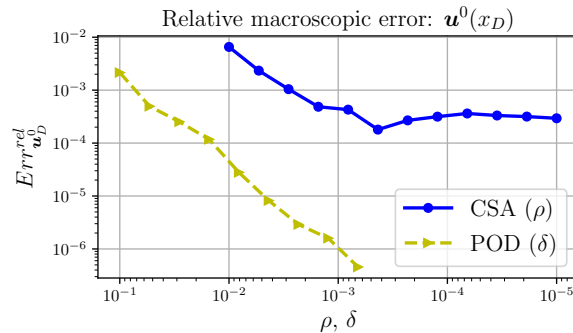


Figure 20: Relative macroscopic error at point D for the CSA and POD algorithm.

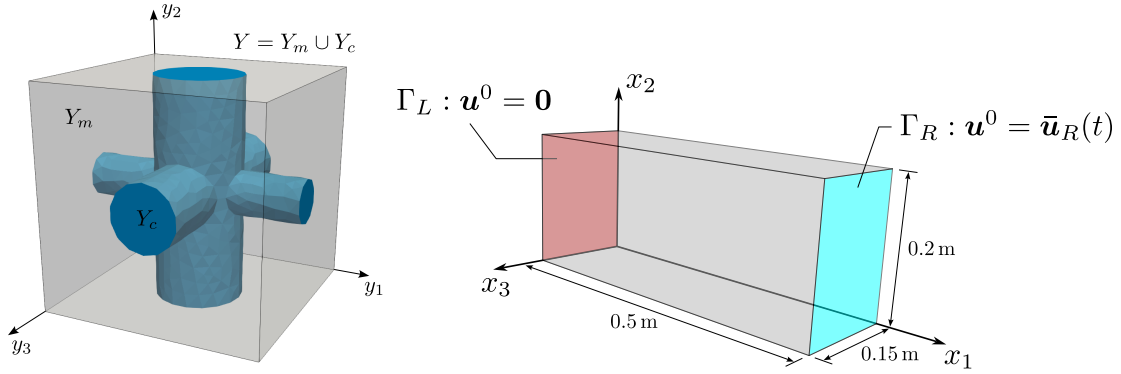


Figure 21: Geometries of the reference unit cell (left) and the macroscopic sample (right).

dimensions $0.5 \times 0.2 \times 0.15$ m is considered, see Fig. 21 (right). One of its faces is fixed, $\mathbf{u}^0 = \mathbf{0}$ on boundary Γ_L , while the opposite face is subjected to prescribed displacements, $\mathbf{u}^0 = \bar{\mathbf{u}}_R(t)$ on Γ_R , where

$$\bar{\mathbf{u}}_R(t_k) = \left(\begin{bmatrix} 1 & 0 & 0 \\ 0 & \cos(\varphi_k) & \sin(\varphi_k) \\ 0 & -\sin(\varphi_k) & \cos(\varphi_k) \end{bmatrix} - \mathbf{I} \right) \mathbf{x}, \quad (51)$$

$$\text{for } \varphi_k = \frac{35}{180} \pi r_k, \quad r_k = \frac{k}{N_t - 1}, \quad \text{and } t_k = r_k \cdot 1 \text{ s}, \quad k = 0, \dots, N_t - 1.$$

The finite element mesh of the macroscopic sample consists of 200 hexahedral Q1 elements, for which a eight-point numerical integration rule is applied.

The reference unit cell representing the periodic microstructure, shown in Fig. 21 (left), is composed of two continuous subdomains with distinct material properties identical to those used in the two-dimensional simulation, see Table 1.

The deformed macroscopic configuration and the reconstructed microscopic structures at selected points are displayed in Fig. 22 for the final loading step. Figures 23 and 24 show the approximation errors of \mathcal{A}_{1133} and \mathcal{S}_{13} at quadrature points A and B for different values of ρ . As the centroid size ρ decreases, the approximation errors become smaller and the number of macroscopic iterations required to achieve equilibrium decreases, as evidenced by the shorter curves for $\rho = 0.001$ and $\rho = 0.0003$.

Figure 25 compares the computational times (left) and the numbers of solved microscopic problems (right) for the CSA simulations and the direct two-scale (FE²) computations. The results confirm that, even for the three-dimensional case, an appropriate choice of the parameter ρ allows a significant reduction of computational cost while maintaining an acceptable level of approximation accuracy.

8. Conclusion

The paper contributes to the field of Model Order Reduction for multiscale computational nonlinear analysis of deforming solids. We have introduced the CSA method for the efficient approximation of homogenized coefficients in hyperelastic media undergoing large deformations. The proposed algorithm relies two ingredients: a) a linear approximation of deformation-dependent homogenized coefficients constructed using representative deformed microstructures and their sensitivities w.r.t. macroscopic strain variations; b) the representative microstructures created “on-flight” during the simulation; for this the clustering of macroscopic deformations based on their distances in metrics of the deformation space is employed. This approach significantly decreases the number of microscopic problems that need to be solved and, hence, the computational cost. Each cluster of macroscopic deformations is represented by a single mean deformation, for which the microscopic problem is solved and the corresponding coefficients, together with their sensitivities with respect to the macroscopic deformation, are computed. These values are then used to approximate the homogenized coefficients for all required macroscopic deformation states. The clustering procedure is dynamic and is repeatedly applied during the iterative solution of the nonlinear problem.

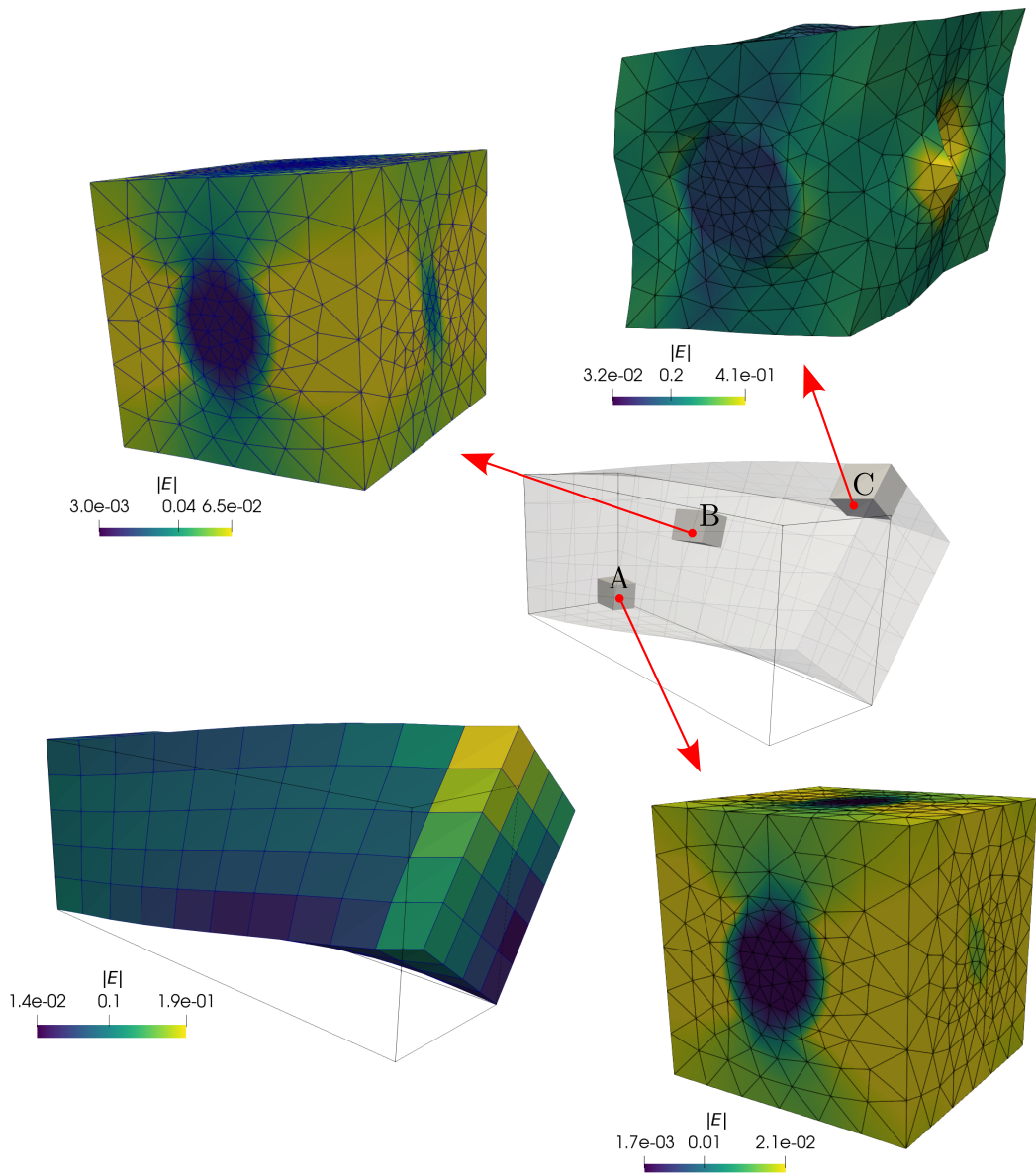


Figure 22: Deformed macroscopic sample and deformed microstructures at selected points.

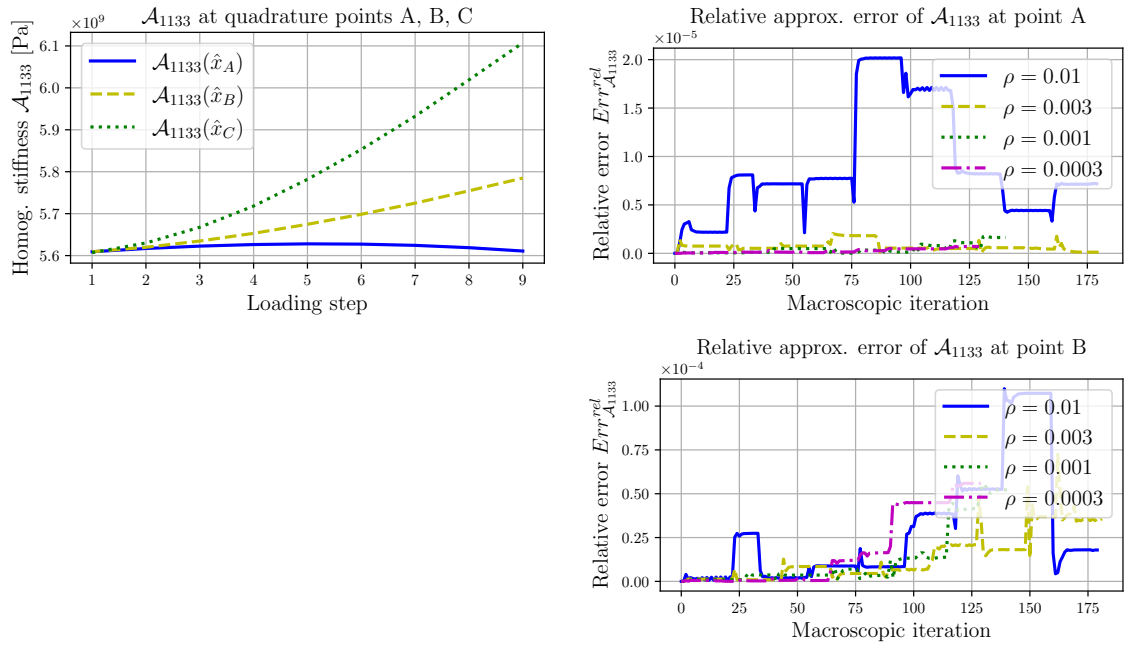


Figure 23: Evolution of the homogenized coefficient \mathcal{A}_{1133} (left) and its relative approximation errors at macroscopic points A and B (right).

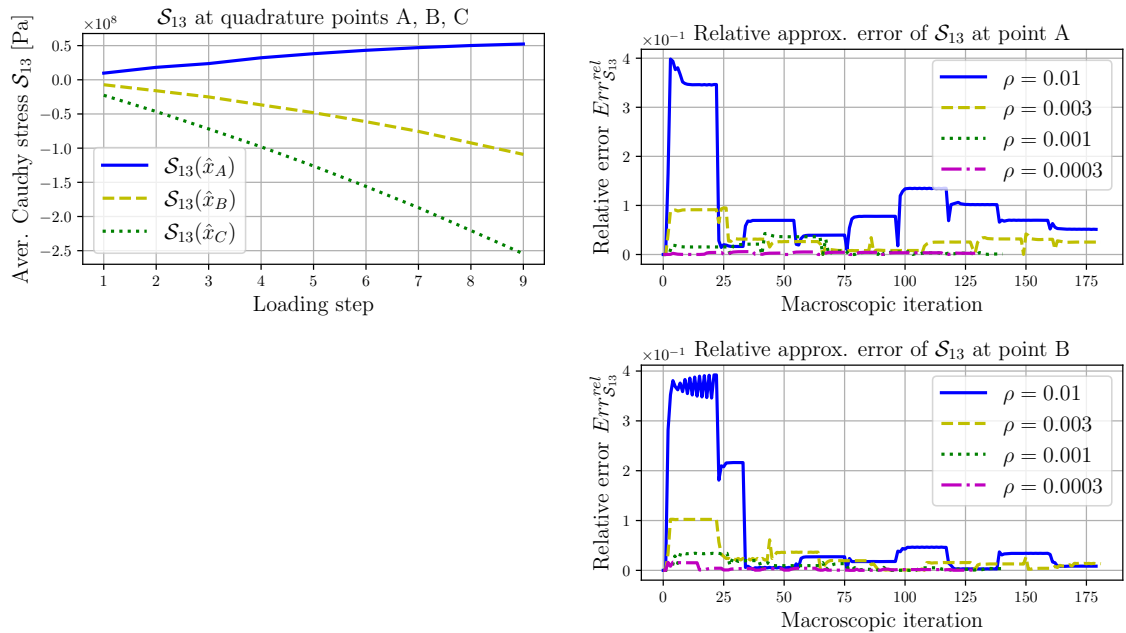


Figure 24: Evolution of the homogenized coefficient \mathcal{S}_{13} (left) and its relative approximation errors at macroscopic points A and B (right).

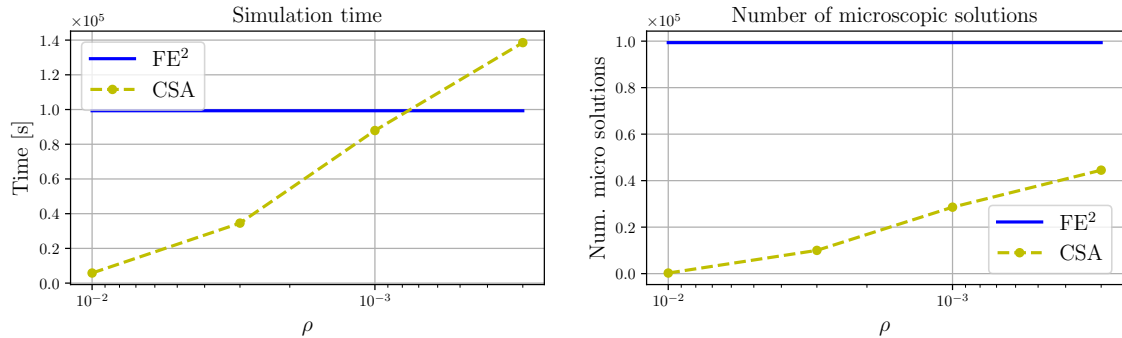


Figure 25: Solution time (left) and number of solved microproblems (right) as functions of ρ .

The computational savings of the CSA algorithm depend on the required approximation accuracy. With increasing accuracy the algorithm efficiency diminishes, as compared the full numerical simulation (FE² approach), primarily because of the overhead associated with evaluating coefficient sensitivities. There is a specific accuracy limit beyond which the time complexity of the CSA method exceeds that of direct two-scale simulation. However, when a fast solution is required and a certain approximation error is acceptable, the CSA method can speed up simulations by several factors. For the numerical example presented in Section 7.3, allowing a relative macroscopic error of approximately 10^{-4} results in a speedup factor of 2.5 compared to the FE² method, which is comparable to the on-line phase of the POD-based simulation.

The efficiency of the CSA approach was also studied with respect to the number of degrees of freedom of the discretized microscopic problem. The computational complexity of the CSA method scales nearly linearly with increasing microscopic resolution, which is a significant advantage over classical proper orthogonal decomposition methods, for which the cost of basis computation grows rapidly. Consequently, the proposed method is suitable for fast approximate simulations of problems with complex microscopic geometries.

The presented CSA method has been tested in the two-scale computational analysis of hyperelastic periodically heterogeneous solids, however, it can be extended with some limitations to account for: a) rate-independent inelastic solids with the constitutive laws involving macroscopic internal variables, b) functionally graded media with “gently varying” microstructures with macroscopic spatial position, hence also to solve two-scale optimization problems, where the required sensitivity analysis of the homogenized coefficients (properties) is naturally treated along with the sensitivity w.r.t. the macroscopic deformation. These issues will be addressed in our further research. Extensions of the CSA method for media characterized by dissipation can be considered on a “heuristic basis”, in analogy with other works that employ macroscopic clustering. However, in our view, the memory effects featuring the time evolution of each local microstructure require tracking all the history, which, in effect, enormously expands the micro-configuration parameterization.

The final remark concerns the potential improvements of the sensitivity-based approximation between neighboring centroids. In this study, we reported a simple method that uses the linear approximation within each centroid for all macroscopic deformation states (MDS) belonging exclusively to one centroid; for MDS points lying in the overlap of several centroids, a blending interpolation is constructed using the weighted linear approximation provided by each of the involved centroids. Further promising improvements have been explored and will be reported in a forthcoming publication devoted also to the above mentioned extensions.

CRediT authorship contribution statement

Vladimír Lukeš: Writing, Visualization, Software, Methodology, Investigation, Conceptualization;

Eduard Rohan: Writing, Formal analysis, Methodology, Investigation, Conceptualization, Funding acquisition, Project administration.

Data Availability

Code and data available at <https://data.mendeley.com/datasets/gvp9kj2nvy/1>.

Declaration of competing interest

The authors declare that they have no known competing financial interests or personal relationships that could have appeared to influence the work reported in this paper.

Acknowledgements

The research has been supported in a part by the grant project GA 2306220S, but mainly by project GA 2412291S of the Czech Science Foundation.

Appendix

We use the shape sensitivity technique and the material derivative approach (see e.g. [35]) to obtain the sensitivity of homogenized coefficient (27) to the configuration transformation corresponding to the microscopic deformation.

Consider a perturbation of material points which is given in terms of a differentiable and Y -periodic vector field $\mathbf{V}(y) : y \mapsto y' \in \mathbb{R}^d$, $y \in Y \subset \mathbb{R}^d$. As explained below, construction of the convection velocity \mathbf{V} is based on the microscopic displacement and deformation fields recovery related to the corrector result of the homogenization. Using \mathbf{V} defined in Y , perturbed configuration $Z(\tau) = \varphi(Y, \tau)$ can be established through mapping $\varphi(y, \tau)$ defined for $y \in Y$, where $\tau \in \mathbb{R}$ is a “time-like” variable. The “material point” position in Y is parameterized by τ , yielding the perturbed coordinates $z(y, \tau)$ defined, as follows

$$\begin{aligned} z_i(y, \tau) &= \varphi_i(y, \tau) := y_i + \tau \mathcal{V}_i(y), \quad i = 1, \dots, d, \\ y_i &= \varphi_i^{-1}(y, \tau) := z_i - \tau \tilde{\mathcal{V}}_i(z), \quad i = 1, \dots, d, \\ Z(\tau) &= \{z \subset \mathbb{R}^d \mid z_i(y, \tau) = \varphi_i(y, \tau), \quad i = 1, \dots, d, \quad y \in Y\}, \\ \mathcal{F}_{ij} &= \partial_j^y \varphi_i = \partial_j^y z_i(y, \cdot). \end{aligned} \tag{52}$$

The inverse mapping $\varphi^{-1}(z, \tau) : z \mapsto y$ is defined in terms of $\tilde{\mathbf{V}}(z(y, \tau))$, such that $\tilde{\mathbf{V}}(z(y, 0)) = \mathbf{V}(y)$. The deformation gradient \mathcal{F}_{ij} is employed in the differentiation of integrals involving gradients $\nabla_y = (\partial_i^y)$ of scalar, or vectorial functions. Using the perturbed configuration and the associated derivatives ∂_i^z , the following holds, where $\hat{(\cdot)} = \partial_\tau(\cdot)|_{\tau=0}$,

$$\begin{aligned} \dot{\mathcal{F}}_{ik} &= \frac{\partial \mathcal{V}_i}{\partial y_k}, \\ \widehat{(\mathcal{F})}_{ik}^{-1} &= -\frac{\partial \mathcal{V}_i}{\partial y_k}, \\ \widehat{\det(\mathcal{F})} &= \nabla_y \cdot \mathbf{V}. \end{aligned} \tag{53}$$

Recalling that the perturbation defined using $\mathbf{V}(y)$ is parametrized by τ , throughout the text below we shall use the notion of the following derivatives: $\delta(\cdot)$ is the total (*material*) derivative, $\delta_\tau(\cdot)$ is the partial (*shape*) derivative with respect to τ . These derivatives are computed as the directional derivatives in the direction of $\mathbf{V}(y)$, $y \in Y$.

Let $u(y)$ be differentiable in Y (whereby u can represent a component of vector field \mathbf{u}), by $\tilde{u}(z, \tau)$ we denote the perturbed function, an image of u thus, defined in Z given by (52)₃. To compute the sensitivity $\delta \mathcal{A}_{klij}$, the partial shape derivative of the strains is required, hence we need

$$\begin{aligned} \delta_\tau(\nabla_y u)_i &= \frac{d}{d\tau} \partial_i^z \tilde{u}(z, \tau)|_{\tau=0} = \frac{d}{d\tau} \left(\frac{\partial u}{\partial y_k} \frac{\partial y_k}{\partial z_i} \right)_{\tau=0} \\ &= \frac{d}{d\tau} \left(\frac{\partial u}{\partial y_k} \left(\delta_{ki} - \tau \frac{\partial \tilde{\mathcal{V}}_k(z)}{\partial z_i} \right) \right)_{\tau=0} = -\frac{\partial \mathcal{V}_k}{\partial y_i} \frac{\partial u}{\partial y_k}, \end{aligned} \tag{54}$$

where (53) was employed. Application of (53) and (54) in the differentiation of the bilinear form (24), leads to (31), where $\delta_\tau \tilde{\mathbf{A}}$ is given by (63).

Sensitivity of the tangential elasticity tensor $\mathcal{A}_{kl ij}$. The sensitivity formula (32) is derived using the partial shape derivative (31) and using the micro-problem (23), where $\mathbf{v} := \boldsymbol{\omega}^{ij} \in \mathbf{H}_{\#}^1(Y)$ can be substituted, so that $a_Y(\boldsymbol{\Xi}^{ij}, \delta\boldsymbol{\omega}^{kl}) = 0$. This yields

$$\begin{aligned}\delta\mathcal{A}_{kl ij} &= \delta_{\tau} a_Y(\boldsymbol{\Xi}^{ij}, \boldsymbol{\Xi}^{kl}) + a_Y(\boldsymbol{\Xi}^{ij}, \delta\boldsymbol{\omega}^{kl} + \delta_{\tau}\boldsymbol{\Pi}^{kl}) + a_Y(\delta\boldsymbol{\omega}^{ij} + \delta_{\tau}\boldsymbol{\Pi}^{ij}, \boldsymbol{\Xi}^{kl}) \\ &= \delta_{\tau} a_Y(\boldsymbol{\Xi}^{ij}, \boldsymbol{\Xi}^{kl}) + a_Y(\delta_{\tau}\boldsymbol{\Pi}^{ij}, \boldsymbol{\Xi}^{kl}) + a_Y(\boldsymbol{\Xi}^{kl}, \delta_{\tau}\boldsymbol{\Pi}^{kl}).\end{aligned}\quad (55)$$

Sensitivity of the effective stress \mathcal{S}_{ij} . The sensitivity of \mathcal{S}_{ij} is obtained using the partial (*shape*) derivative and, namely, making use of (53)₃, so that

$$\delta\mathcal{S}_{ij} = \delta_{\tau} \int_Y \tilde{\boldsymbol{\sigma}} dY = -\mathcal{S} \int_Y \nabla_y \cdot \boldsymbol{\nu} dY + \int_Y \tilde{\boldsymbol{\sigma}} \nabla_y \cdot \boldsymbol{\nu} dY + \int_Y \delta_{\tau} \tilde{\boldsymbol{\sigma}} dY, \quad (56)$$

which yields (33), where $\delta_{\tau} \tilde{\boldsymbol{\sigma}}$ is given by (58).

The partial derivatives of the Cauchy stress tensor $\delta_{\tau} \tilde{\boldsymbol{\sigma}}$ and the associated tangent moduli $\delta_{\tau} \tilde{\mathbf{A}}$ are derived on the basis of the expressions for the Kirchhoff stress $\boldsymbol{\tau} = \mathcal{J} \tilde{\boldsymbol{\sigma}}$ reported in [33]. In particular, the derivative of the Kirchhoff stress $\delta_{\tau} \boldsymbol{\tau}$ is first evaluated,

$$\begin{aligned}\delta_{\tau} \tau_{ij} &= K(2J - 1)J \delta_{ij} \nabla_y \cdot \boldsymbol{\nu} - \frac{2}{3} \mu J^{-2/3} \left(b_{ij} - \frac{1}{3} b_{kk} \delta_{ij} \right) \nabla_y \cdot \boldsymbol{\nu} \\ &\quad + \mu J^{-2/3} \left(\partial_k \mathcal{V}_i b_{kj} + b_{il} \partial_l \mathcal{V}_j - \frac{1}{3} (\partial_k \mathcal{V}_l b_{kl} + b_{kl} \partial_l \mathcal{V}_k) \delta_{ij} \right),\end{aligned}\quad (57)$$

from which the derivative of the Cauchy stress tensor follows as

$$\delta_{\tau} \tilde{\boldsymbol{\sigma}} = \frac{1}{J} (\delta_{\tau} \boldsymbol{\tau} - \boldsymbol{\tau} \nabla_y \cdot \boldsymbol{\nu}). \quad (58)$$

The Truesdell rate of the Kirchhoff stress tensor, denoted by \mathbf{D}^{TK} , is related to the Jaumann rate \mathbf{D}^{JK} through

$$D_{ijkl}^{\text{TK}} = D_{ijkl}^{\text{JK}} - \frac{1}{2} (\delta_{ik} \tau_{lj} + \tau_{il} \delta_{jk} + \delta_{il} \tau_{kj} + \tau_{ik} \delta_{jl}), \quad (59)$$

where the expression for \mathbf{D}^{JK} is derived in [33],

$$\begin{aligned}D_{ijkl}^{\text{JK}} &= K(2J - 1)J \delta_{ij} \delta_{kl} + \mu J^{-2/3} \frac{2}{9} b_{mm} \delta_{ij} \delta_{kl} \\ &\quad + \mu J^{-2/3} \left(-\frac{2}{3} (b_{ij} \delta_{kl} + \delta_{ij} b_{kl}) + \frac{1}{2} (\delta_{ik} b_{lj} + b_{il} \delta_{jk} + \delta_{il} b_{kj} + b_{ik} \delta_{jl}) \right).\end{aligned}\quad (60)$$

Differentiation of the Jaumann rate yields the corresponding derivative $\delta_{\tau} \mathbf{D}^{\text{JK}}$,

$$\begin{aligned}\delta_{\tau} D_{ijkl}^{\text{JK}} &= K(4J - 1)J \nabla_y \cdot \boldsymbol{\nu} \delta_{ij} \delta_{kl} - \frac{2}{3} \mu J^{-2/3} \nabla_y \cdot \boldsymbol{\nu} \left[\frac{2}{9} b_{mm} \delta_{ij} \delta_{kl} - \frac{2}{3} (b_{ij} \delta_{kl} + \delta_{ij} b_{kl}) \right. \\ &\quad \left. + \frac{1}{2} (\delta_{ik} b_{lj} + b_{il} \delta_{jk} + \delta_{il} b_{kj} + b_{ik} \delta_{jl}) \right] \\ &\quad + \mu J^{-2/3} (\partial_m^y \mathcal{V}_r b_{ms} + b_{rm} \partial_m^y \mathcal{V}_s) \left[\frac{2}{9} \delta_{rs} \delta_{ij} \delta_{kl} \right. \\ &\quad \left. - \frac{2}{3} (\delta_{ir} \delta_{js} \delta_{kl} + \delta_{ij} \delta_{kr} \delta_{ls}) + \frac{1}{2} (\delta_{ik} \delta_{lr} \delta_{js} + \delta_{ir} \delta_{ls} \delta_{jk} + \delta_{il} \delta_{kr} \delta_{js} + \delta_{ir} \delta_{ks} \delta_{jl}) \right],\end{aligned}\quad (61)$$

which subsequently allows the computation of the derivative of the Truesdell rate as

$$\delta_{\tau} D_{ijkl}^{\text{TK}} = \delta_{\tau} D_{ijkl}^{\text{JK}} - \frac{1}{2} (\delta_{ik} \delta_{\tau} \tau_{lj} + \delta_{\tau} \tau_{il} \delta_{jk} + \delta_{il} \delta_{\tau} \tau_{kj} + \delta_{\tau} \tau_{ik} \delta_{jl}). \quad (62)$$

Since $\mathbf{D} = \mathbf{D}^{\text{TC}} = \frac{1}{J} \mathbf{D}^{\text{TK}}$ (\mathbf{D}^{TC} is the Truesdell rate of the Cauchy stress tensor) in (13), the shape sensitivity of $\tilde{A}_{ijkl} = D_{ijkl}^{\text{TC}} + \tilde{\sigma}_{jl} \delta_{ik}$ is finally obtained as

$$\delta_{\tau} \tilde{A}_{ijkl} = \frac{1}{J} (\delta_{\tau} D_{ijkl}^{\text{TK}} - D_{ijkl}^{\text{TK}} \nabla_y \cdot \boldsymbol{\nu}) + \delta_{\tau} \tilde{\sigma}_{jl} \delta_{ik}. \quad (63)$$

References

- [1] N. Charalambakis, Homogenization techniques and micromechanics. a survey and perspectives, *Appl. Mech. Rev.* 63 (3) (2010) 030803. doi:10.1115/1.4001911.
- [2] T. I. Zohdi, Homogenization methods and multiscale modeling, in: E. Stein, R. de Borst, T. J. R. Hughes (Eds.), *Encyclopedia of Computational Mechanics*, John Wiley & Sons, Ltd, Chichester, UK, 2017, pp. 1–24. doi:10.1002/9781119176817.ecm2034.
- [3] D. Cioranescu, P. Donato, *An Introduction to Homogenization*, Oxford University Press, 1999. doi:10.1093/oso/9780198565543.001.0001.
- [4] D. Cioranescu, A. Damlamian, G. Griso, *The Periodic Unfolding Method: Theory and Applications to Partial Differential Problems*, Springer Singapore, 2018. doi:10.1007/978-981-13-3032-2.
- [5] V. Lukeš, E. Rohan, Homogenization of large deforming fluid-saturated porous structures, *Comput. Math. Appl.* 110 (2022) 40–63. doi:10.1016/j.camwa.2022.01.036.
- [6] E. Rohan, V.-H. Nguyen, S. Naili, Numerical modelling of waves in double-porosity Biot medium, *Comput. Struct.* 232 (2020) 105849. doi:10.1016/j.compstruc.2017.09.003.
- [7] J. Pinho-da Cruz, J. Oliveira, F. Teixeira-Dias, Asymptotic homogenisation in linear elasticity. part i: Mathematical formulation and finite element modelling, *Comp. Mater. Sci.* 45 (4) (2009) 1073–1080. doi:10.1016/j.commatsci.2009.02.025.
- [8] K. Terada, T. Ito, N. Kikuchi, Characterization of the mechanical behaviors of solid-fluid mixture by the homogenization method, *Comput. Methods Appl. Mech. Eng.* 153 (3–4) (1998) 223–257. doi:10.1016/s0045-7825(97)00071-6.
- [9] E. Rohan, S. Naili, R. Cimrman, T. Lemaire, Multiscale modeling of a fluid saturated medium with double porosity: Relevance to the compact bone, *J. Mech. Phys. Solids* 60 (5) (2012) 857–881. doi:10.1016/j.jmps.2012.01.013.
- [10] E. Rohan, S. Shaw, J. R. Whiteman, Poro-viscoelasticity modelling based on upscaling quasistatic fluid-saturated solids, *Comput. Geosci.* 18 (2014) 883–895. doi:10.1007/s10596-013-9363-1.
- [11] K. Terada, M. Kurumatani, T. Ushida, N. Kikuchi, A method of two-scale thermo-mechanical analysis for porous solids with micro-scale heat transfer, *Comput. Mech.* 46 (2) (2009) 269–285. doi:10.1007/s00466-009-0400-9.
- [12] J. Oden, T. I. Zohdi, Analysis and adaptive modeling of highly heterogeneous elastic structures, *Comput. Methods Appl. Mech. Eng.* 148 (3) (1997) 367–391. doi:10.1016/S0045-7825(97)00032-7.
- [13] M. Wangermez, O. Allix, P.-A. Guidault, O. Ciobanu, C. Rey, Interface coupling method for the global-local analysis of heterogeneous models: A second-order homogenization-based strategy, *Comput. Methods Appl. Mech. Eng.* 365 (2020) 113032. doi:10.1016/j.cma.2020.113032.
- [14] M. G. D. Geers, V. G. Kouznetsova, K. Matouš, J. Yvonnet, *Homogenization Methods and Multiscale Modeling: Nonlinear Problems*, John Wiley & Sons, Ltd, 2017, pp. 1–34. doi:10.1002/9781119176817.ecm2107.
- [15] F. Feyel, A multilevel finite element method (FE2) to describe the response of highly non-linear structures using generalized continua, *Comput. Methods Appl. Mech. Eng.* 192 (28–30) (2003) 3233–3244. doi:10.1016/s0045-7825(03)00348-7.
- [16] J. Schröder, *A numerical two-scale homogenization scheme: the FE2-method*, Springer Vienna, Vienna, 2014, pp. 1–64. doi:10.1007/978-3-7091-1625-8_1.
- [17] J. Yvonnet, Q.-C. He, The reduced model multiscale method (R3M) for the non-linear homogenization of hyperelastic media at finite strains, *J. Comput. Phys.* 223 (1) (2007) 341–368. doi:10.1016/j.jcp.2006.09.019.

- [18] I. Temizer, T. I. Zohdi, A numerical method for homogenization in non-linear elasticity, *Comput. Mech.* 40 (2) (2006) 281–298. doi:10.1007/s00466-006-0097-y.
- [19] F. Fritzen, O. Kunc, Two-stage data-driven homogenization for nonlinear solids using a reduced order model, *Eur. J. Mech. A-solid.* 69 (2018) 201–220. doi:10.1016/j.euromechsol.2017.11.007.
- [20] J. Hernández, J. Oliver, A. Huespe, M. Caicedo, J. Cante, High-performance model reduction techniques in computational multiscale homogenization, *Comput. Methods Appl. Mech. Eng.* 276 (2014) 149–189. doi:10.1016/j.cma.2014.03.011.
- [21] T. Guo, O. Rokoš, K. Veroy, A reduced order model for geometrically parameterized two-scale simulations of elasto-plastic microstructures under large deformations, *Comput. Methods Appl. Mech. Eng.* 418 (2024) 116467. doi:10.1016/j.cma.2023.116467.
- [22] B. A. Le, J. Yvonnet, Q.-C. He, Computational homogenization of nonlinear elastic materials using neural networks, *Int. J. Numer. Meth. Eng.* 104 (12) (2015) 1061–1084. doi:10.1002/nme.4953.
- [23] A. Fadi, S. Elsayed, T. Zohdi, P. Wriggers, Efficient multiscale modeling of heterogeneous materials using deep neural networks, *Comput. Mech.* 72 (1) (2023) 155–171. doi:10.1007/s00466-023-02324-9.
- [24] B. Eidel, Deep CNNs as universal predictors of elasticity tensors in homogenization, *Comput. Methods Appl. Mech. Eng.* 403 (2023) 115741. doi:10.1016/j.cma.2022.115741.
- [25] N. Kovács, M. Maia, I. Rocha, C. Furtado, P. Camanho, F. van der Meer, Physically recurrent neural networks for computational homogenization of composite materials with microscale debonding, *Eur. J. Mech. A-solid.* 112 (2025) 105668. doi:10.1016/j.euromechsol.2025.105668.
- [26] Z. Liu, M. Bessa, W. K. Liu, Self-consistent clustering analysis: An efficient multi-scale scheme for inelastic heterogeneous materials, *Comput. Methods Appl. Mech. Eng.* 306 (2016) 319–341. doi:10.1016/j.cma.2016.04.004.
- [27] S. Wulfinghoff, F. Cavaliere, S. Reese, Model order reduction of nonlinear homogenization problems using a Hashin–Shtrikman type finite element method, *Comput. Methods Appl. Mech. Eng.* 330 (2018) 149–179. doi:10.1016/j.cma.2017.10.019.
- [28] M. A. Benaïmeche, J. Yvonnet, B. Bary, Q.-C. He, A k-means clustering machine learning-based multiscale method for anelastic heterogeneous structures with internal variables, *Int. J. Numer. Meth. Eng.* 123 (9) (2022) 2012–2041. doi:10.1002/nme.6925.
- [29] S. Chaouch, J. Yvonnet, An unsupervised machine learning approach to reduce nonlinear FE2 multiscale calculations using macro clustering, *Finite Elem. Anal. Des.* 229 (2024) 104069. doi:10.1016/j.finel.2023.104069.
- [30] R. Cimrman, V. Lukeš, E. Rohan, Multiscale finite element calculations in Python using SfePy, *Lect. Notes. Pure. Appl.* (2019). doi:10.1007/s10444-019-09666-0.
- [31] V. Lukeš, SfePy: Homogenization of large deforming hyperelastic heterogeneous structures, *Mendeley Data* (2025). doi:10.17632/gvp9kj2nvy.1.
- [32] E. Rohan, V. Lukeš, Modeling large-deforming fluid-saturated porous media using an eulerian incremental formulation, *Adv. Eng. Softw.* 113 (2017) 84–95. doi:10.1016/j.advengsoft.2016.11.003.
- [33] M. Crisfield, *Non-Linear Finite Element Analysis of Solids and Structures, Vol. 2: Advanced Topics*, Wiley, 1991.
- [34] E. Rohan, Sensitivity strategies in modelling heterogeneous media undergoing finite deformation, *Math. Comput. Simulat.* 61 (3-6) (2003) 261–270. doi:10.1016/s0378-4754(02)00082-4.

- [35] J. Haslinger, P. Neittaanmäki, Finite element approximation for optimal shape, material and topology design, Wiley, 1996.
- [36] E. Rohan, V. Lukeš, Modeling nonlinear phenomena in deforming fluid-saturated porous media using homogenization and sensitivity analysis concepts, *Appl. Math. Comput.* 267 (sep 2015). doi:10.1016/j.amc.2015.01.054.
- [37] E. Rohan, V. Lukeš, Homogenized model of peristaltic deformation driven flows in piezoelectric porous media, *Comput. Struct.* 302 (2024) 107470. doi:10.1016/j.compstruc.2024.107470.
- [38] S. Lloyd, Least squares quantization in pcm, *Ieee T. Inform. Theory* 28 (2) (1982) 129–137. doi:10.1109/tit.1982.1056489.
- [39] A. Chatterjee, An introduction to the proper orthogonal decomposition, *Curr. Sci. India.* 78 (7) (2000) 808–817.
- [40] R. Cimirman, SfePy - Write your own FE application (2014). arXiv:1404.6391.
- [41] G. H. Golub, C. F. Van Loan, *Matrix Computations - 4th Edition*, Johns Hopkins University Press, Philadelphia, PA, 2013. doi:10.1137/1.9781421407944.